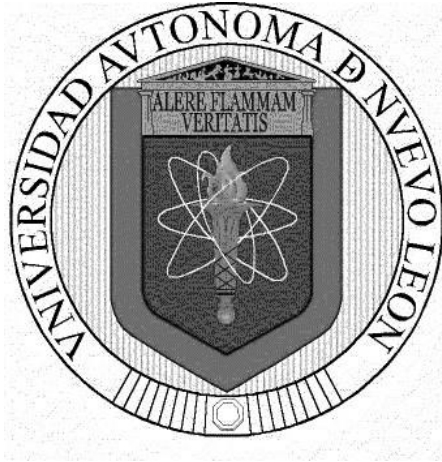**UNIVERSIDAD AUTÓNOMA DE NUEVO LEÓN**

FACULDAD DE CIENCIAS QUÍMICAS

Mathematical model for photocatalytic degradation of emerging pharmaceutical contaminants considering the effect of catalyst reuse and the Six-Flux Model in 2D (SFM -2D) for the estimation of the radiant field

By

Clovis Nchikou

Thesis submitted in partial fulfillment of the requirements for the Degree of Doctor of Philosophy in sciences with orientation in sustainable processes

Monterrey, Nuevo León, 31 August 2022

Thesis: " Mathematical model for photocatalytic degradation of emerging pharmaceutical contaminants considering the effect of catalyst reuse and the Six-Flux Model in 2D (SFM -2D) for the estimation of the radiant field "

Aprobación de la Tesis:

DR. José Ángel Loredo Medrano
Presidente

DRA. Ma Aracely Hernández Ramírez
Secretario (a)

DR. Alejandro Juan Álvarez Guerra
Vocal

DR. Luis Ángel Garza Rodríguez
Vocal

DR. Salvador Tututi Ávila
Vocal

DRA. MARÍA ELENA CANTÚ CÁRDENAS
Sub-Directora de Posgrado

Thesis: " Mathematical model for photocatalytic degradation of emerging pharmaceutical contaminants considering the effect of catalyst reuse and the Six-Flux Model in 2D (SFM -2D) for the estimation of the radiant field "
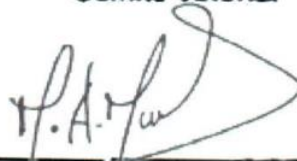
Revisión de la Tesis:

DR. José Ángel Colina Márquez
Co-Asesor

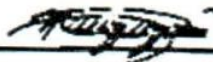DRA. Ma Aracely Hernández Ramírez
Comité Tutorial

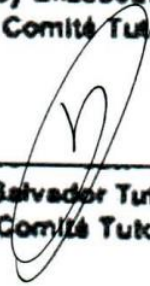DR. Miguel Ángel Mueses
Comité Tutorial

DRA. Nancy Elizabeth Dávila Guzmán
Comité Tutorial

DR. Salvador Tututi Ávila
Comité Tutorial

DRA. MARÍA ELENA CANTÚ CÁRDENAS
Sub-Directora de Posgrado

Abstract

Clovis Nchikou

Date of graduation: August 2022

Universidad Autónoma de Nuevo León

Facultad de Ciencias Químicas

Thesis title: **Mathematical model for photocatalytic degradation of emerging pharmaceutical contaminants considering the effect of catalyst reuse and the Six-Flux Model in 2D (SFM-2D) for the estimation of the radiant field**

Number of pages: 107

Purpose and method of study: This work presents a mathematical model for the photocatalytic degradation of emerging contaminants, considering the effect of the catalyst reuse on a compound parabolic collector (CPC) reactor. The six-flux model in two dimensions (SFM-2D) was coupled to the Ray-Tracing Technique (RTT) for the description and estimation of the radiant field. With the SFM-2D approach, the Radiative Transfer Equation (RTE) was solved in polar coordinates for the formulation of the local volumetric rate of photon absorption (LVRPA), a parameter that describes the light absorption inside the reactor. The LVRPA found with the SFM-2D approach overcomes the limitations faced when adapting the one-dimensional six-flux model (SFM-1D) to tubular reactors and better describes the scattering-absorption behavior inside a tubular reactor than the SFM-1D as well as the overall volumetric rate of photon absorption (OVRPA). It was found that the LVRPA with the SFM-2D decreases from the reactor wall toward the reactor center and that the optimum catalyst loading that leads to the best effectiveness of the photocatalytic activity is between 0.1 and 0.5 g/L. Working outside of this catalyst loading range could lead either to catalyst waste or less efficiency of the photocatalytic process. Five photocatalytic experiments using 10 L of distilled water containing sulfamethoxazole (10 mg/L) at a pH of 6.19 were carried out on a CPC reactor working in recirculation mode using titanium dioxide TiO_2 P25 and varying the catalyst loading (0.1, 0.2, 0.3, 0.4, and 0.5 g/L). The CPC reactor was operating in a turbulent regime under the solar conditions of Monterrey, Mexico. The five experiments reached complete degradation and more than 50 % of the total mineralization after 60 minutes of standardized time (t_{30w}). It was found that the TOC removal increased with the experimental standardized time (t_{30w}). The experiment with 0.3 g/L of catalyst loading was the fastest to reach complete degradation and had the highest mineralization percentage.

Five other experiments were carried out successively under the same conditions (with 0.3 g/L of catalyst loading) by reusing the catalyst to evaluate the effect on SMX degradation. After each cycle of the catalyst reuse, since the catalyst lost its activity, more time (t_{30w}) of reaction was needed to achieve complete degradation, and the TOC removal remained above 50 % after 100 minutes (t_{30w}) of the experiment. To explain this behavior, the optical and physical properties data of the catalyst were collected. The catalyst surface area decreased considerably after the first use (up to 18 %) and slightly varied after each cycle of reuse. The bandgap value dropped to 9.25 % and the specific extinction, scattering, and absorption coefficients also decreased to 77.95, 77.53, and 81.14 % respectively after the 5th cycle. A kinetic model (Langmuir-Hinshelwood type) including the radiant field was used to model the process and was validated with a discrepancy of 6 %. The model predicted that at the seventh cycle of reuse, the catalyst would become useless, and only the photolysis process would remain.

Contribution and conclusions: The LVRPA with the SFM-2D approach overcame the limitations faced when adapting the LVRPA with the SFM-1D on tubular reactors. It predicted the optimum catalyst loading to obtain the best efficiency in the photocatalytic process. The kinetic model presented in this work described the photocatalytic degradation of emerging pharmaceutical contaminants considering the catalyst reuse with a discrepancy of about 6 %. The results showed that the total degradation and more than 50 % of mineralization were obtained. Regarding the model predictions, at the seventh cycle of the catalyst reuse, the photocatalysis process would become useless. The results found in this project could facilitate the connection of the heterogeneous photocatalysis technology to pharmaceutical industries and municipal wastewater treatment plants. This could also help with water treatment, either for its reuse or discharge into our environment without harming living organisms. Finally, it could provide predictions, cost limitations, and optimization of photocatalytic processes at the pilot scale under defined operating conditions.

ADVISOR'S SIGNATURE

Dr. José Ángel Loredo Medrano

ACKNOWLEDGEMENTS

I am very grateful to the Almighty and Most High God, Jesus Christ of Nazareth, who gave me intelligence, strength, wisdom, and health and placed wonderful people on my pathway, helping me to fulfill this great achievement in my life in this very beautiful and kind country, Mexico.

Thanks to the Faculty of Chemical Sciences of the Autonomous University of Nuevo León and CONACyT for the financial support which helped me achieve this purpose.

My thanks to my supervisor, Dr. José Ángel Loredo Medrano, and my co-supervisor, Dr. José Ángel Colina Márquez, for their unconditional support, their patience, and for trusting me.

I'd like to thank Dr. Miguel Ángel Mueses in particular for his assistance in establishing the mathematical modeling and thanks for all of his advice.

With especial thanks to Dr. Aracely Hernández Ramírez, who always acts like a mother and without whom the experimental part of my thesis could not be possible, with the great support of Chemist Jacinto Hernández, also thanks to all the doctors and students of her research group.

I can't forget to say thanks to Dr. Nancy Dávila Guzmán and Dr. Salvador Tututi Ávila, who always gave me their support by asking me pertinent questions related to my thesis and also for their advice.

My thanks to my mother Elisabeth Happy Mbodjo and my father Schmidhauser Walter, my sisters Armande and Verla, my nephews Gaby, Lionel, and Owen, my pastor Yves Roger Medou, and all his family.

A special thanks to families Renteria Fonseca and Samuel Cantú.

Jesus is '' the stone you builders rejected, which has become the cornerstone. Salvation is found in no one else, for there is no other name under heaven given to mankind by which we must be saved. ''

Acts 4: 11-12.

Table of contents

List of figures

List of tables

Nomenclature

$E_{i, i=1,2,3,4,5,6}$	Components of the specific intensity of the radiation (W/m^2)
G	The specific intensity of the radiation (W/m^2)

ω	Scattering albedo coefficient (Dimensionless)
f, b, s	Forward, backward, and sideward scattering probabilities (Dimensionless)
σ, κ	Specific mass scattering and absorption coefficients (m^2/kg)
κ_c	The specific mass absorption coefficient of a given contaminant (m^2/kg)
C_{cat}	Catalyst loading (g/l)
$\dfrac{1}{\lambda_0}$	Photon mean free path length (m)
ψ	The reflectivity of the collector Surface (Dimensionless)
R	Reactor radius (m)
I_0, G_0	Solar incident radiation flux (W/m^2)
$LVRPA$	Local Volumetric rate of photon absorption (W/ m^3)
$LVRPA^{sup}$	Local volumetric rate of photon absorption for the upper hemicylindrical reactor tube (W/ m^3)
$LVRPA^{inf}$	Local volumetric rate of photon absorption for the lower hemicylindrical reactor tube (W/ m^3)
$VRPA/H$	Volumetric rate of photon absorption per unit reactor length (W/m)
$VRPA^{sup}/H$	Volumetric rate of photon absorption per unit reactor length for the upper hemicylindrical reactor tube (W/m)
$VRPA^{inf}/H$	Volumetric rate of photon absorption per unit reactor length for the lower hemicylindrical reactor tube (W/m)
$OVRPA$	Overall volumetric rate of photon absorption (W)
N	Number of consecutive reflections

CPC	Compound Parabolic Collector
Tub	Tubular reactor
C_{cpc}	CPC concentrator factor
θ_{cpc}	Half acceptance CPC angle
r, θ	Radial and angular coordinates
HG	Henyey-Greenstein phase function
DR	The diffuse reflectance phase function
L	Lambert's cosine law
SMX	Sulfamethoxazole
TOC	Total organic carbon
k_{app}	Apparent kinetic constant
r_C	Reaction rate (ppm/min)
C	Substrate concentration (ppm)
t_{30W}	Standardized time (minutes)
v_R	Reaction volume (m^3)
v_T	Total volume (m^3)
C_0	Initial substrate concentration (ppm)
L	Cell length (cm)
$\omega_{corr}, \lambda_{\omega_{corr}}, \gamma, a_\lambda, b_\lambda$	SFM parameters
λ	Wavelength (nm)
T_λ	Transmittance
R_λ	Reflectance
N-Reuse, N-Fresh	Number of cycles of the catalyst reuse
ψ	Reflexivity of the CPC reflectors
ξ	Average incidence angle
n_p	Number of particles per unit volume
a_p	The projected area of one catalyst particle

SFM-1D-HG	**Six Flux Model in 1 dimension with HG phase function without Lambert's cosine law**
SFM-1D-DR	**Six Flux Model in one dimension with DR phase function without Lambert's cosine law**
SFM-1D-HG-L	**Six Flux Model in 1 dimension with HG phase function with Lambert's cosine law**
SFM-1D-DR-L	**Six Flux Model in 1 dimension with DR phase function with Lambert's cosine law**
SFM-2D-HG	**Six Flux Model in 2 dimensions with HG phase function without Lambert's cosine law**
SFM-2D-DR	**Six Flux Model in 2 dimensions with DR phase function without Lambert's cosine law**
SFM-2D-HG-L	**Six Flux Model in 2 dimensions with HG phase function with Lambert's cosine law**
SFM-2D-DR-L	**Six Flux Model in 2 dimensions with DR phase function with Lambert's cosine law**

1. Introduction

Nowadays, water scarcity is growing in the world due to its contamination by diverse types of pollutants coming from different sources, the constant increase in the human population, the expansion of cities, and the high development of industries. The growth of industries has caused many chemicals to end up in our environment. Among those pollutants, emergent recalcitrant contaminants (ERC) are present. The European Commission defined ERC as ''substances that have the potential to enter the environment and cause adverse ecological and human health effects but are still largely unregulated and whose fate and potential effects are poorly understood'' [1]. ERC are synthetically and naturally occurring substances that

are not regulated in environmental monitoring programs but also might be candidates for upcoming regulations because of their detrimental effects and persistence. Pharmaceuticals, endocrine disruptors, surfactants, personal care products, micro/nanoparticles, pesticides, personal care products, sweeteners, hormones, and illicit drugs are some of the ERC. They are resistant to degradation, and the conventional ways of water treatment are not capable of handling this because of their presence in very small concentrations in water (nano or micrograms per liter) [2]. The difference between pharmaceuticals and other ERC is their high degree of stability and the capacity to maintain their biological effects at low concentrations [3;4], which makes them very harmful to our environment. Fortunately, advanced oxidation processes (AOPs) are adequate for degrading pollutants classified as non-biodegradable or with low biodegradability, persistence, and high chemical stability [5]. The challenges for the remediation of contaminated effluents consist in ensuring the quality and safety of the water discarded into natural water bodies. In Mexico, the National Water Commission (CNA) is in charge of monitoring the legal framework established by the Official Mexican Standards (NOM). The Ministry of Health and Assistance (SSA) and the Ministry of Environment and Natural Resources (SEMARNAT) are the secretariats that contain and carry out the studies. One of the impediments of the NOM is the lack of regulation of emerging pollutants, and this recent issue has been studied and debated constantly all over the world (Ambriz E. et al., 2014; Melissa Valdez-Carrillo et al.,2020).

1.1. Emerging pharmaceutical contaminants and heterogeneous photocatalysis

1.1.1. Emerging pharmaceutical contaminants

ERC end up in our environment in many ways without being controlled and regulated, but fortunately, their detection has been made possible by improved analytical techniques (Barroso et al., 2019). Pharmaceuticals are the most serious among ERC, characterized by their high degree of stability and the capacity to maintain their biological effects at low concentrations [3;4]. The origins of the pollution of the environment by pharmaceuticals are several, such as the exponential increase of pharmaceutical industries and the lack of

an efficient method of treatment of pharmaceutical wastewater. Other sources are the high and uncontrolled consumption of drugs in human and veterinary medicines as well as the lack of storage of pharmaceutical residues (Aus der Beek et al., 2016; Kot-Wasik et al., 2016). Although pharmaceuticals are found at low levels, their constant release into the environment might lead to high long-term concentrations and generate negative effects on living organisms (Liu et al., 2017; Mezzelani et al., 2018). Table 1 illustrates some pharmaceuticals with their respective concentrations.

Table. 1 Some emerging pharmaceutical contaminants and their concentrations (R. Sivaranjanee and P.S. Kumar., 2021).

ECR detected	Concentration range	References
Ibuprofen	4–2370 ng/l	Roberts and Thomas (2006)
Acetaminophen	38.9 ng/l	Shraim et al. (2017)
Metformin	15.2 ng/l	Shraim et al. (2017)
SMX	7–965 ng/l	Elliott et al. (2018)
Cephalexin	1.88 ng/l	Shraim et al. (2017)
Diclofenac	0.096 µg/l	Montagner and Jardim (2011)
Naproxen	<10 ng/l	Zhang et al. (2008)

1.1.1.1 Effect of pharmaceuticals on human health and the ecosystem

Humans are directly affected by pharmaceuticals by actively taking medicine or indirectly by environmental exposure, mainly by the consumption of contaminated food and drinking water. Humans are also indirectly exposed to pharmaceuticals by contaminated soils, dust, and surface waters from swimming (A. B. A. Boxall, in Health Care and Environmental Contamination, Elsevier, 2018, pp. 123–136), (Fig 1). Even though there are numerous trace levels of pharmaceuticals in drinking water, the concentrations found are unlikely to present a significant risk to human health individually. Nevertheless, it was found trace levels of gemfibrozil, sulfamethoxazole, and diclofenac in drinking water from the United States of America at levels suggesting that they may pose a low level of concern (G. M. Bruce et al., 2010, World Health Organization, Pharmaceuticals in drinking water, World Health Organization, Geneva, Switzerland, 2012). The presence of antibiotics such as sulfamethoxazole and ciprofloxacin in surface water and soil can lead to the development of antimicrobial-resistant bacteria, fungi, and biofilm in natural environments [1], which may cause serious problems for living organisms' health.
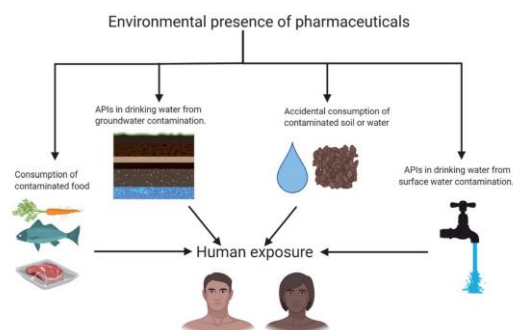
Fig. 1 Routes of human exposure to pharmaceuticals, APIs: Active pharmaceutical ingredients [1].

It was found that antimicrobial-resistant bacteria present in fish from aquaculture have been shown to transmit their resistance to humans (G. Rhodes et al., 2000), but an additional investigation should be

conducted since this transfer is fully unknown. Sulfamethoxazole can be classified as highly toxic to photosynthetic organisms, in particular aquatic plants, algae, and cyanobacteria (P. Kovalakova et al., 2020). The work conducted by N. Martins et al. in 2012 concluded that ciprofloxacin is a risk for the most sensitive aquatic ecosystems. Gemfibrozil is reported to be an endocrine disruptor that has been shown to decrease testosterone levels in goldfish by 49 %, and it has also been shown to increase oxidative stress in mollusks (L. Araujo et al. 2011; G. McEnef et al. 2015). Diclofenac has high biological activity, which can potentially be toxic to non-target organisms (M. Parolini et al. 2020) and has been shown to cause oxidative stress and affect carbohydrate and fatty acid metabolism in C. pyrenoids at low concentrations (Y. Zhang et al. 2019). Only a few cases of pharmaceuticals and their effects on humans and the ecosystem are cited here, but the list remains exhaustive and well discussed in the literature (A. Gogoi et al. (2018)).

1.1.2. Heterogeneous photocatalysis

AOPs are based on the generation of radicals (hydroxyl radicals mainly), which are non-selective and very efficient when treating pollutants. AOPs for water and wastewater treatment include photolysis and photocatalysis, ozonation, Fenton and photo-Fenton, ultrasound radiation, sonolysis, electrochemical oxidation, and wet air oxidation [5]. Photocatalysis is composed of homogeneous and heterogeneous photocatalysis. The former is the liquid or gaseous phase, and the latter is more than one phase.

During the last forty years, heterogeneous photocatalysis has been attracting significant attention, especially as a "green" and sustainable technology for the elimination of toxic and nonbiodegradable species both present in gaseous and liquid phases [6].
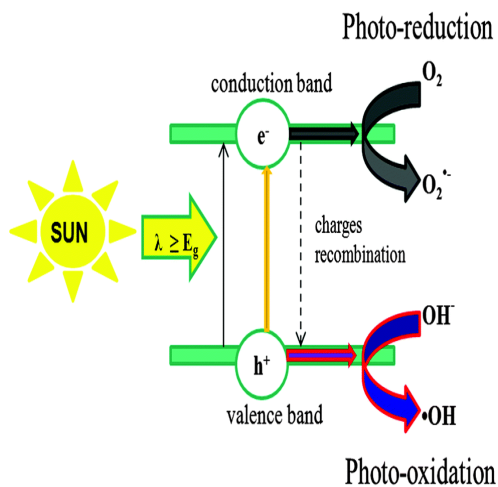
Fig 2. Photocatalysis mechanism [7].

The photocatalytic mechanism illustrated in Figure 2 is based on the photoexcitation of a semiconductor with energy equal to or greater than the energy of its bandgap for the promotion of electrons from the valence (VB) to the conduction (CB) band, leaving vacant sites named holes; then, in the presence of water or oxygen molecules, oxidized species such as radical hydroxyl are produced. Those radicals are non-selective and very efficient for pollutant degradation.
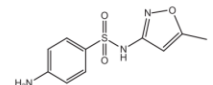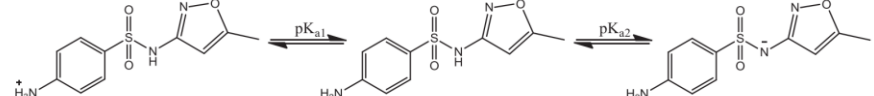
It is worth mentioning that if there are no donors/receptors to react immediately with electron/hole pairs formed, the recombination process occurs, leading to the liberation of heat, which disfavors the process. The most commonly used catalyst is titanium dioxide (TiO_2) because of its abundance in nature, its good physical and optical properties, and its high photocatalytic activity. It is biologically and chemically inert, inexpensive, and non-toxic even though its main limitation is its activity only in the UV light region [5]. Many studies reported regarding the photocatalytic degradation of pharmaceuticals are frequently reduced to the use of TiO_2 as the main photocatalyst due to its good photocatalytic properties cited above [5].

1.1.3. Sulfamethoxazole (SMX)

Sulfamethoxazole (SMX), used as a model compound in this study, is a synthetic antibiotic, one of the most commonly used sulfonamide antibiotics in humans and veterinary medicine [8]. It has been used to treat diseases and infections and in feed additives to promote the growth rate and weight gain of food animals (A. Kumar et al., 2010). It has been detected in aquatic environments such as surface water, rivers, and groundwater at different concentration levels (F.A. Caliman et al., 2009; L. Liu et al., 2013). SMX and its metabolites are excreted in urine and directed with wastewater to treatment plants where they are not fully degraded [8]. Many studies on SMX degradation under solar and artificial light based on TiO_2 have been published [5;9;10]. Xekoukoulotakis, N. P et al., [9] performed the photocatalytic SMX degradation and mineralization at SMX initial concentrations between 2.5 and 30 mg/L, with six commercially available TiO_2 catalysts at loadings between 100 and 750 mg/L. They found that Degussa P25 was highly active, i.e. nearly complete SMX degradation and mineralization could be achieved after 30 and 120 min of reaction, respectively at 10 mg/L SMX and 250 mg/L catalyst concentrations. On the other hand, Diego Alejandro Pino Sandoval et al., [10] studied the SMX and acetaminophen (ACP) photocatalytic degradation and mineralization based on two commercial TiO_2 catalysts, Degussa P25 and KronoClean 7000, at different catalyst amounts, under simulated and natural solar irradiation for the solution of 10 mg L^{-1} initial concentration of each drug. The results showed complete degradation of the mixture and abatement of 70% of the initial TOC concentration in distilled water with Degussa P25 (1.0 g L^{-1}) using both radiation sources at 400 kJ m^{-2} of the UV accumulated energy.

The physical and chemical characteristics of SMX are listed in Table 2.

Table 2. physicochemical characteristics of SMX (Chengdu Qi et al. 2014).

Molecular structure	Formula	Molecular weight	Solubility	pK_a
	$C_{10}H_{11}N_3O_3S$	253.28	0.61 g/L	p$K_{a1,2}$ = 1.6,5.7

1.2. Modeling of the photocatalytic process

The modeling of any process remains an essential and fundamental tool since it helps with predictions, cost reduction, and optimization of some parameters to operate in appropriate conditions and improve process efficiency. Thus, the modeling of the photocatalytic process also contributes to sustainability. When modeling a photocatalytic process, some factors should be considered, such as the type of photocatalytic reactor, the radiant field, hydrodynamics, and chemical species transport throughout the reactor. These aspects influence the local rate of generation of electron/hole pairs and hence the local kinetic rate of degradation of pollutants in water. Figure 3 shows an example of a scheme to follow when modeling such a process that considers three components: i) the radiant field that must be described considering the light source, whether it is natural or artificial, and then solving the radiative transfer equation (RTE); ii) hydrodynamics; and iii) reaction kinetics involving quantum yield and mass balance (Ochoa Gutiérrez et al., 2018). In this work, a great effort was concentrated on the radiant field.
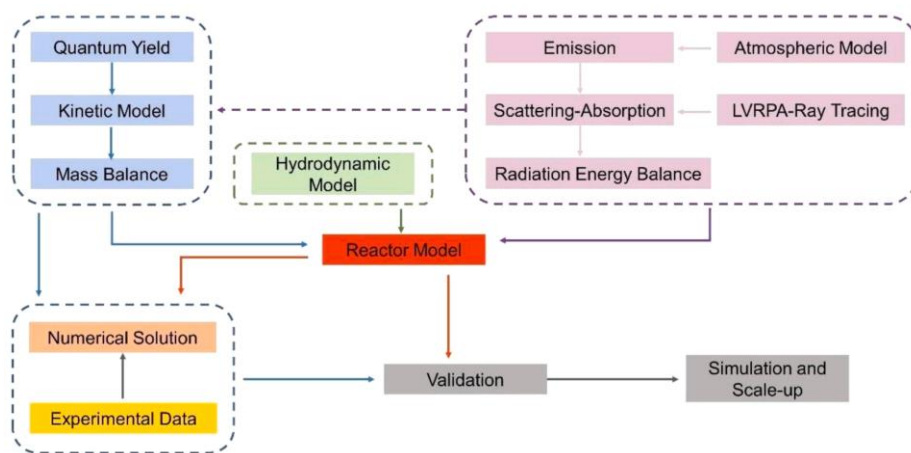
Fig. 3. Methodological approach to modeling of a photocatalytic reactor. adapted from

(Ochoa-Gutiérrez et al., 2018).

1.3. The radiant field

Heterogeneous photocatalysis, a method for cleaning water and air, is still attracting a lot of interest. The use of solar radiation to directly supply UV photons to the process makes this a very environmentally friendly method. Solar heterogeneous photocatalysis is a rising development that can address environmental issues [11–12]. Sunlight harvesting and a photoreactor capable of completely using UV rays are necessary for full-scale deployment of the technology. Furthermore, the intrinsic kinetics of the photocatalytic reaction must be derived using a model of UV light absorption (photons absorbed) in the reactor volume. The difficulty of this endeavor is determined by the reactor's shape and the photon source utilized to stimulate photocatalytic processes [13]. For practical applications in photocatalytic processes, it is vital to adopt a model that can be applied to a wide range of reactor geometries using basic mathematics. To calculate the local volumetric rate of photon absorption (LVRPA), however, equations describing the radiant field and photon absorption must be developed. One of the most difficult components of the LVRPA computation is modeling light scattering due to the presence of solid particles suspended in the liquid [14]. Solar photocatalytic reactors remain a complex and unsolved problem due to the geographical

heterogeneity, the type of solar radiation propagation (direct and diffuse), and the integral-differential nature of the RTE [14–16]. This statement refers to the various light-traversing events (absorption, scattering) that can occur. The intrinsic photocatalytic rate law can be established using the LVRPA, which is derived from the RTE. The steady-state RTE is depicted in Eq. (1), which has no temperature dependence:

$$\frac{dI_\lambda(S,\Omega)}{ds} = -\kappa_\lambda I_\lambda(S,\Omega) - \sigma_\lambda I_\lambda(S,\Omega) + \frac{\sigma_\lambda}{4\pi}\int_{\Omega=4\pi} P(\Omega' \to \Omega)I_\lambda(S,\Omega')d\Omega' \tag{1}$$

where I_λ is the photon irradiance (W/m^2), κ_λ the absorption coefficient (m^2/kg), σ_λ the scattering coefficient (m^2/kg), $P(\Omega' \to \Omega)$ the scattering phase function, λ the wavelength (m), S the spatial coordinate (m), and Ω the solid directional angle (Steradian) [17].

The radiation field is dependent on the optical properties of the suspension, the reactor type, and the geometric design of the reactor while solving the RTE. [15] Several approximate solutions to the RTE have been proposed by methods such as quadrature, spherical harmonics, the repeating one [20], and Monte Carlo simulation [21]. However, these methods all demand a very high degree of accuracy and a very long processing period. Analytical solutions closer to the RTE's exact solution have been proposed as a result of the restrictions outlined above. According to Theissing et al. [23], the dispersed radiation from spherical particles can only go in two directions: forward and backward. Assuming radiation from a single dispersion with a direct component and a spread isotropic component, Fritz and colleagues [24] developed the Two Stream Model (TSM). With the Six Flux Model (SFM), Chu and Churchill [25] assumed only six discrete components to represent the angular distribution for dispersion: forward, backward, and four sideways. As a result, it was possible to reduce the original integral-differential transport equation to six differential equations based on discrete components of the particular intensity. This set of equations can be applied to a wide range of geometries. These equations can be solved in a fraction of the time thanks to their simple

algebraic structure. To estimate the radiant field in a fat plate reactor, Brucato et al. [26] employed the SFM technique, called SFM-1D (or SFM-DR-1D to emphasize the diffuse reflectance phase function). Symmetry was introduced along the z-axis and Monte Carlo simulations were used to compare their results to the Monte Carlo simulations. The SFM provides a more accurate solution to the RTE than the Two Flux Model (TFM). There are six directions in which a photon can be spread using the SFM technique. Before its use in energy dispersion systems, this model described heat transport in a variety of open environments. In an annular photoreactor, Li Puma et al. [30] employed the SFM to estimate the LVRPA. To model the radiant field in a solar CPC, Colina-Márquez et al. [13] used the SFM-DR-1D in conjunction with the Ray-Tracing approach for the first time. It was utilized by Acosta-Herazo et al. [31] to analyze and optimize the radiation absorption in solar photocatalytic reactors using the SFM-1D with the Henyey-Greenstein (HG) phase function. SFM-DR-1D was used to generate Eq. (2), which represents the LVRPA developed by Brucato et al. [26].

$$LVRPA = \frac{I_0\left(\left(\omega_{corr}-1+\sqrt{1-(\omega_{corr})^2}\right)e^{-\frac{x}{\lambda_{\omega_{corr}}}}+\gamma\left(\omega_{corr}-1-\sqrt{1-(\omega_{corr})^2}\right)e^{\frac{x}{\lambda_{\omega_{corr}}}}\right)}{\lambda_{\omega_{corr}}\omega_{corr}(1-\gamma)} \tag{2}$$

where I_0 is the photon flux.

The parameters of the SFM-DR-1D, such as the extinction length $\lambda\omega_{corr}$, the corrected scattering albedo ω_{corr}, and γ are calculated from the optical properties of the suspended photocatalyst particles. The x variable represents the position in the incident flux trajectory at which the photon flux is being measured. The SFM-DR-1D and SFM-HG-1D made the following assumptions for calculating the LVRPA:

    i)   The distribution of photocatalytic particles is perfect.

    ii)   Absorption by reactor fluid or material has been ignored.

    iii)   Only UV photons belonging to the absorption range of the catalyst (295-384 nm) are considered.

    iv)   The system's optical properties did not change.

v)   The surface's reflectance is regarded as constant over time.

The scattering albedo is estimated in Eq. 3.:

$$\omega = \frac{\sigma}{\sigma+k} \tag{3}$$

The scattering and absorption coefficients are referred to as σ and κ, respectively. The extinction coefficient is the sum $\sigma +\kappa$ of the extinction coefficients. According to Eqs. (4-6), the adjusted scattering albedo is determined using the probabilities of scattering forward, backward, and sideways [26].

$$a = 1 - \omega f - \frac{4\omega^2 s^2}{(1-\omega f-\omega b-2\omega s)} \tag{4}$$

$$b = \omega b + \frac{4\omega^2 s^2}{(1-\omega f-\omega b-2\omega s)} \tag{5}$$

$$\omega_{corr} = \frac{b}{a} \tag{6}$$

The values found for f, b, and s (scattering probabilities forward, backward, and sidewards, respectively) differ from one phase function to another [26, 27]. Eqs. (7–10) depict the estimation of the other optical parameters of the SFM-1D [32]:

$$\tau = (\sigma^* + \kappa^*)c_{cat}\delta \tag{7}$$

$$\tau_{app} = a\tau\sqrt{1 - (\omega_{corr})^2} \tag{8}$$

$$\lambda_{\omega_{corr}} = \frac{1}{a(\sigma^*+\kappa^*)c_{cat}\sqrt{1-(\omega_{corr})^2}} \tag{9}$$

$$\gamma = \frac{1-\sqrt{1-(\omega_{corr})^2}}{1+\sqrt{1-(\omega_{corr})^2}}e^{-2\tau_{app}} \tag{10}$$

where c_{cat} is the catalyst loading, δ the estimated reactor thickness when the photon flux collides directly with the reactor wall, σ^* and κ^* are the catalyst-specific mass scattering and absorption coefficients, respectively. Secondly, the parameters σ and κ are equal to $\sigma^* c_{cat}$ and $\kappa^* c_{cat}$, respectively.

In terms of reactors, the SFM application is practical, with easy numerical procedures and short computation times [33]. Slab photoreactors are well-suited for use with Brucato's SFM, whereas tubular photoreactors are not quite as well-suited. To estimate the radiant field in these tubular geometries, it is important to adjust the SFM-1D with the discretization of the CPC reactor cross-sectional area. Concerning the computation of the overall volumetric photon absorption (OVRPA), this discretization had an impact. In previous work, Colina-Márquez et al. [13] showed LVRPA profiles of CPC reactors with various catalyst loads. They used the SFM in conjunction with ray-tracing to estimate the radiant field. With the ray-tracing technique, Acosta-Herazo et al. [31; 34] used more than 100 rays, and found a higher OVRPA than Colina-Márquez et al. [13]. Because of the processing demands and the disparities in the OVRPA calculations, the discretization of the reactor space is a considerable difficulty. The absence of LVRPA experimental data for solar CPC reactors has prevented the accurate estimate of the radiant field, which is a second obstacle to overcome. These problems have prompted the search for a different mathematical technique that delivers a more precise solution. So, an obvious alternative to address these issues is an analytical answer. However, it is not possible to implement this kind of solution in the original RTE form. The consideration of boundary conditions is the next important concern. Radiation reaching a plane surface does not vary from one point to the next, but that is not the case for a curved surface. As the impact beam strikes the surface, its incidence angle changes from one point to the next, causing the incoming radiation to vary. As far as we can tell, the

reported studies on this topic did not consider Lambert's cosine law or radiation absorption by fluids for measuring radiant fields in CPC photoreactors [13, 31, 34, 36, 37, 38, 39]. When Lambert's cosine law is taken into account as a boundary condition, the SFM results are more in line with the RTE solution [40]. In this paper, we suggested an analytical solution to the RTE based on a novel two-dimensional Six-Flux Model (SFM-2D). Starting with the SFM, we developed a simple algebraic expression for a two-dimensional system with polar coordinates. We also accounted for Lambert's cosine law and the radiation absorption by the fluid when estimating the radiant field in a CPC photoreactor. Final comparisons included LVRPAs obtained using various phase functions (SFM-DR-2D and SFM-HG-2D), as well as those obtained using Lambert's cosine law (SFM-2D-L) and those obtained without it (SFM-2D-L) (SFM-2D).

1.4. Reaction kinetics

A strong understanding of the possible chemical reactions occurring during the photocatalytic process is required to formulate the rate law equation that can suitably describe the photocatalytic process mechanisms. Some possible steps may occur during the photocatalytic process: 1) The activation step represents the promotion of the electron from the VB to the CB of the catalyst after it receives energy equal to or greater than its bandgap energy to form electron/hole pairs, 2) e^-/h^+ pair recombination3) Pollutant migration toward the catalyst surface4) Adsorption step, in which several chemical species from the bulk, such as water, oxygen molecules, or the contaminant, can be adsorbed on the catalyst surface.5) Reaction at the interface of solid and liquid. Here, after the species have been adsorbed, redox reactions occur at the catalyst surface. 6) The desorption of the substrates from the catalyst surface and, 7) The migration toward the bulk. Following the possible steps listed above, many researchers, such as Turchi and Ollis (1990), have derived a kinetic model which usually contains the incident light and a mathematical structure similar to the Langmuir-Hinshelwood (L-H) expression but with different phenomenological meanings.

Table. 3. Some kinetic models used from 2002 to 2021 (D. Wang et al (2021)).

Rate law	Water pollutants	Catalyst	Reactor configuration	Reference
$r_i = -\alpha_1 \sqrt{\widehat{E}^a_{g(\lambda\to\lambda')}}\,\theta_i^{L-H}$	Trichloroethylene	TiO_2	Flat plate photoreactor	Brandi et al., 2002
$r_i = -\alpha_1 \sqrt{\widehat{E}^a_{g(\lambda\to\lambda')}}\,\theta_i^{L-H}$	Isoproturon, Simazine and Propazine	TiO_2	Annular photoreactor	Toepfer et al., 2006
$r_i = -\alpha_1 \left[-1 + \sqrt{1 + \alpha_2 \widehat{E}^a_{g(\lambda\to\lambda')}}\,\right]\theta_i^{L-H}$	4-chlorophenol	TiO_2 and TiO_2/SiO_2	Annular photoreactor	Satuf et al., 2008
$r_i = -\alpha_1 \left[-1 + \sqrt{1 + \alpha_2 \widehat{E}^a_{g(\lambda\to\lambda')}}\,\right]\theta_i^{L-H}$	Cyanide	TiO_2	Cylindrical photoreactor	Marugán et al., 2008
$r_i = -\alpha_1 \left[-1 + \sqrt{1 + \dfrac{\alpha_2}{C_i}\widehat{E}^a_{g(\lambda\to\lambda')}}\,\right]C_i$	Dichloroacetic acid	TiO_2	Parallelepiped photoreactor	Ballari et al., 2008
$r_i = \{\alpha_1\phi C_i + \alpha_2[1 - \phi\sqrt{C_i}]\}\sqrt{\widehat{E}^a_{g(\lambda\to\lambda')}}$ where $\phi = \alpha_3 C_{i,0}[1 - \alpha_4 \widehat{E}^a_{g(\lambda\to\lambda')}\,t]$	Oxalic acid	TiO_2	Fluidized bed photoreactor	Pozzo et al., 2010
$r_i = -\alpha_1 \left[-1 + \sqrt{1 + \alpha_2 \widehat{E}^a_{g(\lambda\to\lambda')}}\,\right]\theta_i^{L-H}$	1,4-dioxane, hormone disrupting estrogens (E1, E2, EE2, E3), propanal, dichloroacetic acid, phenol, chlorophenols, methylphenols, 2,4-dichlorophenoxy-acetic acid (2,4-D), diuron and ametrine	TiO_2	Tubular reactor with compound parabolic collector (CPC)	Mueses et al., 2013
$r_i = \{\alpha_1\phi C_i + \alpha_2[1 - \phi\sqrt{C_i}]\}\sqrt{\widehat{E}^a_{g(\lambda\to\lambda')}}$ where $\phi = \alpha_3 C_{i,0}[1 - \alpha_4 \widehat{E}^a_{g(\lambda\to\lambda')}\,t]$	Oxalic acid	TiO_2	Annular photoreactor	Grčić and Li Puma, 2013
$r_i = -\alpha_1 \sqrt{\widehat{E}^a_{g(\lambda\to\lambda')}}\,\theta_i^{L-H}$	Herbicides mixture (2,4-D, diuron, and ametrine)	TiO_2	Tubular reactor with compound parabolic collector (CPC)	Colina-Márquez et al., 2015
$r_i = -\alpha_1 \sqrt{\widehat{E}^a_{g(\lambda\to\lambda')}}\,\theta_i^{L-H}$	4-Nitrophenol	TiO_2	Cylindrical photoreactor	Palmisano et al., 2015
$r_i = \alpha_1\left(-1 + \sqrt{1 + \alpha_2 \widehat{E}^a_{g(\lambda\to\lambda')}}\,\right)C_i$	Formic acid	TiO_2	Parallelepiped photoreactor	Camera-Roda et al., 2016
$r_i = -\alpha_1\left(-1 + \sqrt{1 + \alpha_2 \widehat{E}^a_{g(\lambda\to\lambda')}}\,\right)C_i$	Clofibric acid	TiO_2	Cylindrical photoreactor with two circular flat windows	Manassero et al., 2015
$r_i = \{\alpha_1\phi C_i + \alpha_2[1 - \phi\sqrt{C_i}]\}\sqrt{\widehat{E}^a_{g(\lambda\to\lambda')}}$ where $\phi = \alpha_3 C_{i,0}[1 - \alpha_4 \widehat{E}^a_{g(\lambda\to\lambda')}\,t]$	Oxalic acid	TiO_2	Annular photoreactor	Turolla et al., 2016
$r_i = -\alpha_1 \sqrt{\widehat{E}^a_{g(\lambda\to\lambda')}}\,\theta_i^{L-H}$	2-hydroxybenzoic acid	TiO_2 and $Ag@TiO_2$	Annular and channel photoreactors	Grčić and Li Puma, 2017
$r_i = -\alpha_1 \left[-1 + \sqrt{1 + \alpha_2 \widehat{E}^a_{g(\lambda\to\lambda')}}\,\right]\theta_i^{L-H}$	Phenol	TiO_2	Cylindrical photoreactor	Tolosana-Moranchel et al., 2017
$r_i = -\alpha_1\left(-1 + \sqrt{1 + \alpha_2 \widehat{E}^a_{g(\lambda\to\lambda')}}\,\right)$	Methanol	TiO_2	Annular photoreactor	Casado et al., 2017
$r_i = -\alpha_1 \sqrt{\widehat{E}^a_{g(\lambda\to\lambda')}}\,C_i$	Clofibric acid	TiO_2	Planar microreactor with immobilized catalyst	Satuf et al., 2019
$r_i = -\alpha_1 \left[-1 + \sqrt{1 + \alpha_2 \widehat{E}^a_{g(\lambda\to\lambda')}}\,\right]\theta_i^{L-H}$	Clofibric acid	TiO_2-rGO	Cylindrical photoreactor	Tolosana-Moranchel et al., 2019
$r_i = \theta_i^{L-H}\dfrac{q_{inc}}{1 + \alpha_1 q_{inc}}$	Arsenite	TiO_2	NETmix reactor with immobilized catalyst (BSI and FSI)	Santos et al., 2021

These models are usually based on the assumption that hydroxyl radicals are the predominant oxidizing species. However, other species such as holes may also serve as primary oxidative species (Li et al., 2012; Sahu et al., 2018 b). Table 3 shows some kinetic models used in the literature taken from D. Wang et al. (2021) where $\alpha_{i=1,2\cdots,N}$ are the rate law constants, $\hat{E}_{g(\lambda\to\lambda')}$ is the overall volumetric rate of photon absorption (OVRPA, Einstein/m^{3}s), θ_i^{L-H} is Langmuir-Hinshelwood function (dimensionless), C_i is the concentration, $C_{i,0}$ is the initial reactant concentration, and q_{inc} is the incident radiation. Turchi and Ollis' (1990) model was improved years later by estimating the absorption-scattering of the light in the reaction system, named the local volumetric rate of photon absorption (LVRPA). To achieve that, the radiative transfer equation (RTE) was solved, either by using rigorous methods such as the discrete ordinate method or by using an analytical method such as the two, four, or six flux model, but it still needs improvement. One of the objectives of this study is to improve the estimation of the absorption-scattering in the reactive system with a realistic and simplistic method. This has been discussed further in this work. The kinetic model used in this study is similar to that used by Brandi et al., 2002, Toepfer et al., 2006, Colina-Márquez et al., 2015, Palmisano et al., 2015, Grcic et al.,2017, and Satuf et al., 2019 (see Table 3).

1.5. The catalyst reuse

Catalyst reuse is continuously receiving great attention nowadays since it can contribute significantly to minimizing the operational cost of the photocatalysis process for wastewater treatment. There are several studies on catalyst reuse at the laboratory scale in the literature [41; 42; 43], and only a few at the pilot scale (P. Fernández-Ibáñez et al., 2003; José Colina-Márquez et al., 2009). Nevertheless, none of these studies has established a mathematical model for the photocatalytic process considering catalyst reuse. After reusing a catalyst several times, it loses its photocatalytic activity. It would then be useful to know after how many cycles of use the catalyst is no longer photo effective. The catalyst's surface area, as well as its capacity for absorbing light, may be reduced due to some byproducts generated during the photocatalysis process that remain on its surface, occupying active sites. It would be interesting to get

information about the catalyst's physical and optical properties, such as the specific absorption and scattering coefficients since these appear in the LVRPA mathematical expression. This would help to better interpret how the photocatalytic degradation of a defined contaminant is affected after various cycles of catalyst reuse.

1.6. Photocatalytic solar reactors

A photocatalytic solar reactor is a reactor where photocatalytic reactions are carried out on a solar scale. Without radiation, the photocatalytic process could not happen since its initiation step is the excitation of a catalyst with adequate energy. Thus, it is imperative to build a suitable photoreactor that can fully use UV photons.

Different types of photoreactors have been designed over time. Two principal distinctions have been made: concentrating and non-concentrating photoreactors, slurry, and fixed catalyst reactors. Non-concentrating photoreactors use solar radiation as it arrives at the earth's surface while concentrating photoreactors are designed with an optical system to augment the radiative flux impinging on the reactor (Camilo A. Arancibia-Bulnes et al., 2009). Usually, concentrating photoreactors capture the incident solar radiation energy either to transform it into heat (thermal energy) or directly into electricity (photovoltaic cells), and non-concentrating photoreactors collect solar radiant energy to carry out photochemical processes (photolysis, photocatalysis, etc.). The first concentrated photoreactors used were parabolic trough concentrators (PTC) with one- or two-axis tracking systems to track the sun's movement in the sky (see Figure 4). These reactors were designed to work as thermal collectors and then were adapted as photocatalytic reactors by replacing the absorber tube with a Pyrex glass tube (Alpert et al., 1991; Minero et al., 1993). Nevertheless, they were found to be energetically less efficient and more expensive than non-concentrating photoreactors (Malato et al., 1997).

Figure. 4. Parabolic trough photocatalytic reactor at Plataforma solar de Almeria (Spain) (Malato et al., 2007).

PTC reactors have many advantages, such as being small while receiving an important amount of energy per unit volume, working in a turbulent regime, and volatile compounds do not evaporate. Their main disadvantages are that they use direct radiation and a very small fraction of diffuse radiation and are expensive with low optical and quantum efficiencies. Another disadvantage is that they require tracking systems that are costly, require maintenance and consume energy (Camilo A. Arancibia-Bulnes et al., 2009). There are some non-concentration reactors we can cite as falling film reactors (Bockelmann et al., 1995; Gernjak et al., 2004), the shadow pond reactor (Bedford et al., 1994), the flat tubular reactors (Goswami et al., 1997), the flat plastic reactors (van Well et al., 1997), multistep cascade falling-film reactors (Guillard et al., 2003; Pichat et al., 2004), and CPC reactors (Blanco et al., 1999) (Figure 5 a). Usually, non-concentrating collectors do not need solar tracking devices, which makes them cheaper than PTC reactors (Camilo A. Arancibia-Bulnes et al., 2009). Their installation is easier, and their manufacturing costs are cheaper since their components are simpler, which implies easy and low-cost maintenance. Since they are static, the surface needed for their installation is small (Camilo A. Arancibia-Bulnes et al., 2009).

Non-concentrating CPC reactors have caught the attention of many researchers since they combine both the PTC and non-concentrator reactor advantages and are found to be efficient in their use in photocatalytic processes at the pilot scale (Malato Rodriguez et al., 2004). They have only a few disadvantages, such as a small concentration and the multiple reflections of solar rays on the CPC reflectors before reaching the reactor receiver (reactor tube) (Figure 5 b). Several investigations are related to CPC photoreactors (S. Malato et al., 2002; Camilo A. Arancibia-Bulnes et al., 2009; D. K. Patel., 2017).

As pointed out earlier, another established difference is between slurry and supported catalyst photoreactors. In slurry photoreactors, the catalyst particles are suspended in water and provide a larger contact surface area per unit mass and per unit radiant flux. Nevertheless, the main drawback of this type of photoreactor is the catalyst recovery. Meanwhile, the catalyst recovery is easier but with less contact surface area per unit mass and per unit radiant flux when the catalyst particles are fixed (Camilo A. Arancibia-Bulnes et al., 2009; S. Danfá et al., 2021).
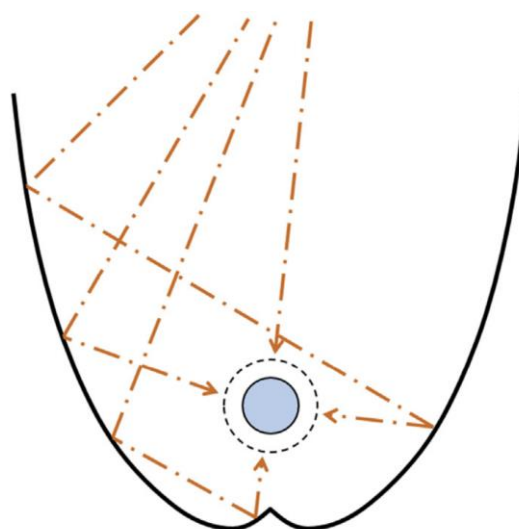
a)   b)

Figure. 5. Compound parabolic collector (a) Esteban García, A. B. et al., 2020, b) M. Orosz, and R. Dickes., 2017).

1. Hypothesis

The mathematical model obtained will predict the photocatalytic degradation of emerging pharmaceutical contaminants, considering the effect of catalyst reuse and estimating the radiant field with the Six-Flux Model in 2D (SFM-2D).

2. Main goal

To develop a mathematical model using a Six-Flux Model in 2D (SFM-2D) to describe the radiant field in a CPC reactor, as well as a kinetic model for the solar photocatalytic degradation of emerging pharmaceutical contaminants while taking into account the effect of the catalyst's physical and optical properties changing due to loss of activity after several uses.

3. Specific goals

- To formulate a Six-Flux Model in 2D (SFM-2D) for analyzing the absorption and photon scattering to estimate the LVRPA.

- To evaluate the LVRPA performance regarding the change of the optical properties due to the loss of the active surface of the catalyst.

- To propose a kinetic model that considers the catalyst reuse factor in the solar photocatalytic degradation of emerging pharmaceutical contaminants (sulfamethoxazole is taken as the contaminant model) in wastewater.

- To validate the mathematical model experimentally with a pilot-scale CPC reactor for the degradation of emerging pharmaceutical contaminants under different operating conditions.

4. Area of opportunity and contribution

There is a lack of studies on mathematical modeling of the photocatalytic process considering the catalyst reuse at the pilot scale in the literature. This project could facilitate the association of heterogeneous photocatalysis technology with pharmaceutical industries and municipal wastewater treatment plants to treat water either for its reuse or discharge into our environment without harming living organisms. This study could also help with predictions, cost limitations, and optimization of photocatalytic processes at the pilot scale under defined operating conditions.

5. Methodology

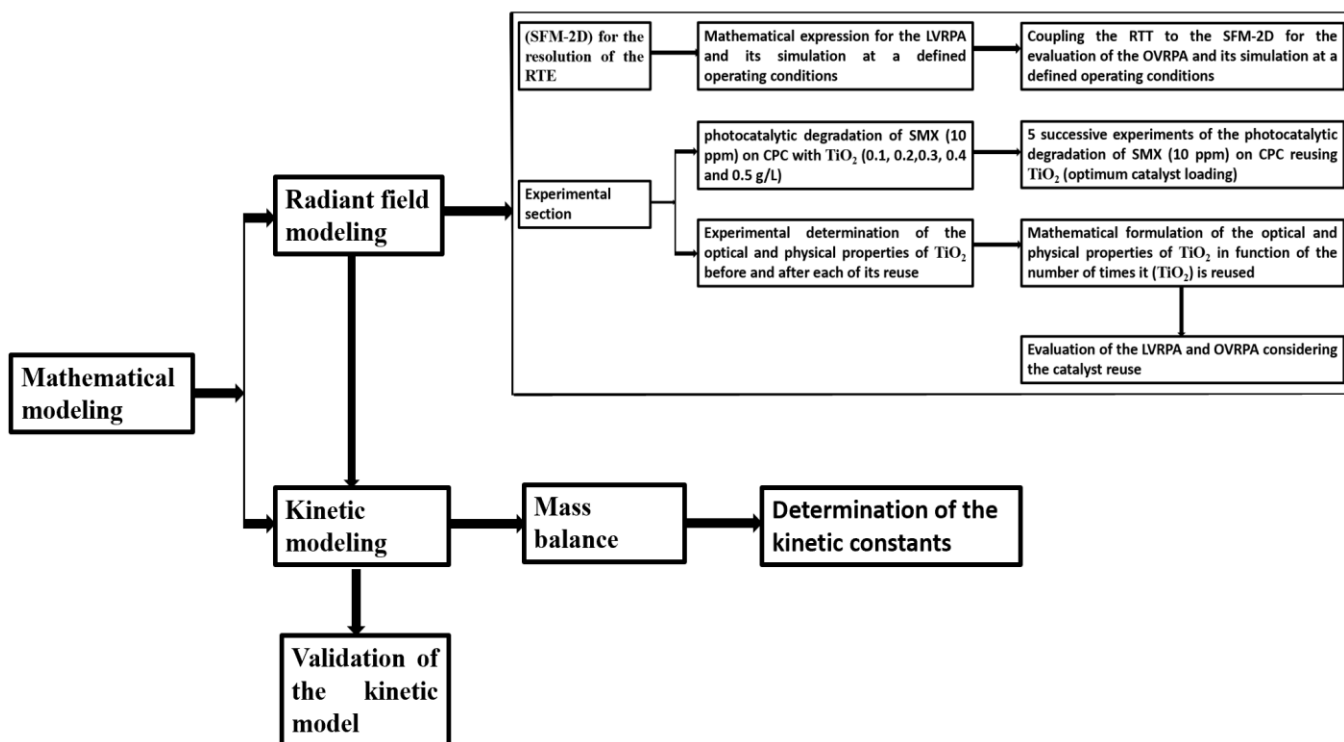The methodology of this project is divided into two parts as graphically presented in Figure 6.

Fig. 6. General scheme of the methodology.

The first part consists of modeling the radiant field by solving the RTE with the SFM-2D approach to derive a mathematical expression of the LVRPA. Once the LVRPA is found, the Ray-Tracing technique (RTT) will be coupled to the SFM-2D for the calculation of the OVRPA, and then, the LVRPA and the OVRPA will be simulated. The simulation of the LVRPA and the OVRPA helps to find the interval where the optimum catalyst loading which leads to the highest photocatalytic efficiency belongs (this was found between 0.1 and 0.5 g/L). The next thing will be the experimental validation of the radiant field by performing five photocatalytic experiments on a CPC reactor for the degradation of SMX under the same operating conditions except for varying the catalyst concentration from 0.1 to 0.5 g/L (0.1, 0.2, 0.3, 0,4 and 0.5 g/L). After finding the optimum catalyst loading, five other experiments will be done sequentially under the same operating conditions as previously, except for reusing the catalyst. After each experiment, the catalyst's optical and physical properties will be determined and then introduced into the LVRPA and OVRPA to see how these can be affected and how much they can influence the kinetic. The second part of the project consists of proposing a mathematical model considering the catalyst reuse, then performing the mass balance in the CPC reactor and the determination of the kinetic constants. Finally, the entire model will be validated by experimental data.

The recapitulation of the steps to follow for the establishment of the mathematical model in this project:

1) Radiant Field Modeling: formulation and solving of the SFM and coupling with boundary conditions:

i)   The Definition of the Six-Flux-Model (SFM) for the resolution of the RTE: In the (SFM) approach, only the symmetry along the z-axis should be considered and an analytic expression should be provided for cylindrical geometry,

ii) Coupling the SFM with the Ray-Tracing technique to determine a more accurate expression of the LVRPA,

iii) Calculation with a higher approximation of the Overall Volumetric of Photon Absorption (OVRPA),

2) Modeling for the determination of the catalyst's optical properties,

3) Evaluation of the LVRPA considering catalyst reuse,

4) The kinetic model and mass balance,

5) Numerical solution for simulation and model validation with experimental data (This project will be carried out using the software MATLAB).

7. Modeling of the radiant field

7.1. The SFM derivation

Brucato et al. [26] used identical techniques to derive the LVRPA in polar coordinates with this innovative SFM (SFM-2D). However, the SFM-2D two-dimensionality and the fluid's absorption of radiant radiation differ from each other. As previously stated, the original SFM assumes that photons disperse after interacting with a particle in any of the six cartesian directions for the incoming radiation (Figure 7). The name Six-Flux-Model refers to the fact that there are six distinct photon fluxes (SFM).
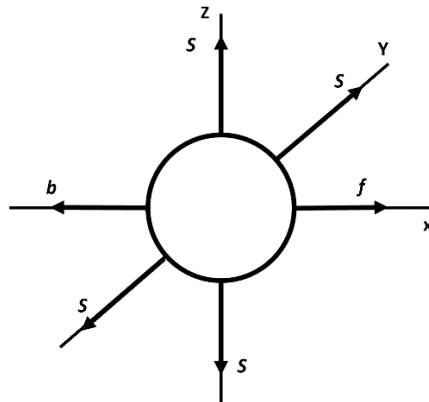
Fig. 7. Six Flux Model scattering directions.

An analytical LVRPA expression was developed in this study to solve RTE in polar coordinates with an SFM technique (SFM-2D), and the energy balance in a specified control volume was performed, as shown in Figure 8. The following assumptions guide the SFM-2D model employed in this study:

- Radius R and thickness 2R of an indefinitely long annular photoreactor;

- Particles that are big and widely separated are consistent with geometric optics.

- Particles of varying sizes and distributions are considered;

- Radiation can be absorbed by the fluid;

- The heterogeneous system does not produce any emissions;

- Only scattering or absorption occurs when a photon collides with a particle, and the scattering probability is determined by the catalyst albedo ω;

- Figure 7 shows that the scattering event can only occur in six of the cartesian coordinates;

- Scattered particles are likely to be scattered in any one of the four directions on a plane normal to the entering direction, but their forward and backward probabilities f and b are different, as shown in Figure 7.
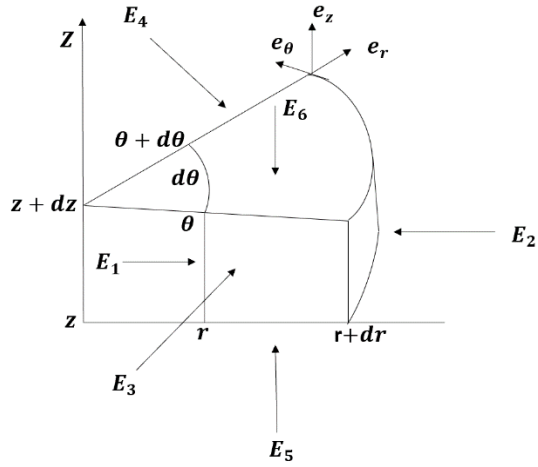
Fig. 8. Differential model for the radiant energy balance.

The photon balance in a volume of a cylinder as shown in Figure 8 leads to:

$$r\partial\theta\partial z E_1|_{r+dr} = r\partial\theta\partial z E_1|_r - r\partial\theta\partial z E_1(1-\omega)n_p a_p \partial r -$$

out   *in*   *absorbed*

$$r\partial\theta\partial z E_1\omega(b+4s)n_p a_p \partial r +$$

Scattering out

$$r\partial\theta\partial z E_2\omega(b)n_p a_p \partial r + \partial r\partial z E_3\omega(s)n_p a_p r\partial\theta + \partial r\partial z E_4\omega(s)n_p a_p r\partial\theta +$$

$$r\partial r\partial\theta E_5\omega(s)n_p a_p \partial z + r\partial r\partial\theta E_6\omega(s)n_p a_p \partial z$$

Scattering in   (11)

Where n_p is the number of particles per unit volume, a_p is the projected area of one particle, ω is the single albedo of the particle, f, b, and s are the forward, backward, and sidewise-scattering probabilities respectively which match Eq. (12)

$$f + b + 4s = 1 \tag{12}$$

Rearranging and dividing the equation (11) by $r\partial r\partial\theta\partial z$ and tending ∂r to zero, and performing the same way a photon balances in the other directions, one obtains the set of the following six equations:

$$\frac{\partial(rE_1)}{r\partial r} = \frac{1}{\lambda_0}[(-1+\omega f)E_1 + \omega bE_2 + \omega s(E_3+E_4+E_5+E_6)] \tag{13}$$

$$\frac{\partial(rE_2)}{r\partial r} = \frac{1}{\lambda_0}[(+1 - \omega f)E_2 - \omega b E_1 - \omega s(E_3 + E_4 + E_5 + E_6)] \tag{14}$$

$$\frac{\partial(E_3)}{r\partial\theta} = \frac{1}{\lambda_0}[(-1 + \omega f)E_3 + \omega b E_4 + \omega s(E_1 + E_2 + E_5 + E_6)] \tag{15}$$

$$\frac{\partial(E_4)}{r\partial\theta} = \frac{1}{\lambda_0}[(+1 - \omega f)E_4 - \omega b E_3 - \omega s(E_1 + E_2 + E_5 + E_6)] \tag{16}$$

$$\frac{\partial(E_5)}{\partial z} = \frac{1}{\lambda_0}[(-1 + \omega f)E_5 + \omega b E_6 + \omega s(E_1 + E_2 + E_3 + E_4)] \tag{17}$$

$$\frac{\partial(E_6)}{\partial z} = \frac{1}{\lambda_0}[(+1 - \omega f)E_6 - \omega b E_5 - \omega s(E_1 + E_2 + E_3 + E_4)] \tag{18}$$

Where E_1, E_2, E_3, E_4, E_5 and E_6 represent the six discrete components of the specific radiation intensity (In this case E_2 is the incident beam, see Figure 1), $f, b,$ and s represent the forward-scattering, backward-scattering, and sidewise-scattering probabilities, respectively. $f, b,$ and s are calculated using an adequate phase function which describes suitably the catalyst particle behavior, λ_0 is the photon mean free path. $\frac{1}{\lambda_0}$ is equal to $n_p a_p$ and also defined as $(\sigma^* + \kappa^*)c_{cat} + \kappa_c^* C_c$ where σ^* and κ^* are the catalyst-specific mass absorption and scattering coefficients respectively, κ_c^* is the specific mass absorption coefficient of a given contaminant, C_c is the contaminant concentration and C_{cat} is the catalyst loading. E_5 and E_6 are equal because of the symmetry consideration since the photon flux was supposed to be constant in the Z direction.

The assumption of an infinitely large system for symmetry consideration results in:

$$\frac{\partial(E_5)}{\partial z} = \frac{\partial(E_6)}{\partial z} = 0 \tag{19}$$

Eqs. (19), (16) and (17) give:

$$E_5 = E_6 = \frac{\omega s(E_1 + E_2 + E_3 + E_4)}{1 - \omega f - \omega b} \tag{20}$$

Introducing Equation (20) into Equations (13), (14), (15) and (16) one obtains:

$$\frac{\partial(rE_1)}{r\partial r} = -C_1 E_1 + C_2 E_2 + C_3(E_3 + E_4) \tag{21}$$

$$\frac{\partial(rE_2)}{r\partial r} = -C_2 E_1 + C_1 E_2 - C_3(E_3 + E_4) \tag{22}$$

$$\frac{\partial(E_3)}{r\partial \theta} = -C_1 E_3 + C_2 E_4 + C_3(E_1 + E_2) \tag{23}$$

$$\frac{\partial(E_4)}{r\partial \theta} = -C_2 E_3 + C_1 E_4 - C_3(E_1 + E_2) \tag{24}$$

$$C_1 = \frac{1}{\lambda_0}\left(1 - \omega f - \frac{2(\omega s)^2}{1 - \omega f - \omega b}\right) \tag{25}$$

$$C_2 = \frac{1}{\lambda_0}\left(\omega b + \frac{2(\omega s)^2}{1-\omega f-\omega b}\right) \tag{26}$$

$$C_3 = \frac{1}{\lambda_0}\left(\omega s + \frac{2(\omega s)^2}{1-\omega f-\omega b}\right) \tag{27}$$

Using equation Eq. (20) the value of $E_5 = E_6$ is deduced. So, Eq. (21) implies:

$$\frac{\partial^2(rE_1)}{\partial r^2} = -C_1\frac{\partial(rE_1)}{\partial r} + C_2\frac{\partial(rE_2)}{\partial r} + C_3\left(\frac{\partial(rE_3+rE_4)}{\partial r}\right) \tag{28}$$

Eq. (21-22) into Eq. (28) implies:

$$\frac{\partial^2(rE_1)}{\partial r^2} = -C_1\left(-C_1 rE_1 + C_2 rE_2 + C_3(rE_3+rE_4)\right) +$$

$$C_2\left(C_2 rE_1 + C_1 rE_2 - C_3(rE_3+rE_4)\right) + C_3\left(\frac{\partial(rE_3+rE_4)}{\partial r}\right) \tag{29}$$

$$\frac{\partial^2(rE_1)}{\partial r^2} = \left(C_1{}^2 - C_2{}^2\right)rE_1 - C_3(C_1 + C_2)(rE_3 + rE_4) + C_3\left(\frac{\partial(rE_3+rE_4)}{\partial r}\right) \tag{30}$$

Eq. (22) implies:

$$\frac{\partial^2(rE_2)}{\partial r^2} = C_2 \frac{\partial(rE_1)}{\partial r} - C_1 \frac{\partial(rE_2)}{\partial r} - C_3 \left(\frac{\partial(rE_3 + rE_4)}{\partial r}\right) \tag{31}$$

Eq. (21-22) into Eq. (31) implies:

$$\frac{\partial^2(rE_2)}{\partial r^2} = -C_2\big(-C_1 rE_1 + C_2 rE_2 + C_3(rE_3 + rE_4)\big) +$$

$$C_1\big(C_2 rE_1 + C_1 rE_2 - C_3(rE_3 + rE_4)\big) - C_3 \left(\frac{\partial(rE_3 + rE_4)}{\partial r}\right) \tag{32}$$

$$\frac{\partial^2(rE_2)}{\partial r^2} = \big(C_1{}^2 - C_2{}^2\big)rE_2 - C_3(C_1 + C_2)(rE_3 + rE_4) - C_3 \left(\frac{\partial(rE_3 + rE_4)}{\partial r}\right) \tag{33}$$

Eq. (23) implies:

$$\frac{\partial^2(E_3)}{\partial\theta^2} = -C_1 \frac{\partial(rE_3)}{\partial\theta} + C_2 \frac{\partial(rE_4)}{\partial\theta} + C_3 \left(\frac{\partial(rE_1 + rE_2)}{\partial\theta}\right) \tag{34}$$

Eqs. (23-24) into Eq. (34) implies:

$$\frac{\partial^2(E_3)}{\partial\theta^2} = -C_1 r\big(-C_1 rE_3 + C_2 rE_4 + C_3(rE_1 + rE_2)\big) +$$

$$C_2 r\big(C_2 rE_3 + C_1 rE_4 - C_3(rE_1 + rE_2)\big) + C_3 \left(\frac{\partial(rE_1 + rE_2)}{\partial\theta}\right) \tag{35}$$

$$\frac{\partial^2 (E_3)}{\partial \theta^2} = \left(C_1{}^2 - C_2{}^2\right)r^2 E_3 - C_3(C_1 + C_2)r(rE_1 + rE_2) + C_3\left(\frac{\partial(rE_1 + rE_2)}{\partial \theta}\right)$$ (36)

Eq. (24) implies:

$$\frac{\partial^2 (E_4)}{\partial \theta^2} = C_2 \frac{\partial(rE_3)}{\partial \theta} - C_1 \frac{\partial(rE_4)}{\partial \theta} - C_3\left(\frac{\partial(rE_1 + rE_2)}{\partial \theta}\right)$$ (37)

Eqs. (23-24) into Eq. (37) implies:

$$\frac{\partial^2 (E_4)}{\partial \theta^2} = -C_2 r\big(-C_1 rE_3 + C_2 rE_4 + C_3(rE_1 + rE_2)\big) +$$

$$C_1 r\big(C_2 rE_3 + C_1 rE_4 - C_3(rE_1 + rE_2)\big) - C_3\left(\frac{\partial(rE_1 + rE_2)}{\partial \theta}\right)$$ (38)

$$\frac{\partial^2 (E_4)}{\partial \theta^2} = \left(C_1{}^2 - C_2{}^2\right)r^2 E_4 - C_3(C_1 + C_2)r(rE_1 + rE_2) - C_3\left(\frac{\partial(rE_1 + rE_2)}{\partial \theta}\right)$$ (39)

Eq. (30) + Eq. (33) and Eq. (36) + Eq. (33) give respectively:

$$\frac{\partial^2 (f)}{\partial r^2} = Af - 2Brg$$ (40)

$$\frac{\partial^2 (g)}{\partial \theta^2} = Agr^2 - 2Bfr$$ (41)

where,

$$f = rE_1 + rE_2 \tag{42}$$

$$g = E_3 + E_4 \tag{43}$$

$$A = C_1{}^2 - C_2{}^2 \tag{44}$$

$$B = C_3(C_1 + C_2) \tag{45}$$

Eq. (40) implies:

$$g = \frac{A}{2Br}f - \frac{1}{2Br}\frac{\partial^2(f)}{\partial r^2} \tag{46}$$

Eq. (46) into Eq. (41) gives:

$$\frac{\partial^2\left(\frac{A}{2Br}f - \frac{1}{2Br}\frac{\partial^2(f)}{\partial r^2}\right)}{\partial \theta^2} = A\left(\frac{A}{2Br}f - \frac{1}{2Br}\frac{\partial^2(f)}{\partial r^2}\right) - 2Bfr \tag{47}$$

Eq. (47) implies:

$$A \left(\frac{r^2 \partial^2 f}{\partial r^2} + \frac{\partial^2 f}{\partial \theta^2} \right) - \frac{\partial^2 \left(\frac{\partial^2 (f)}{\partial r^2} \right)}{\partial \theta^2} - r^2 \left(A^2 - 4B^2 \right) f = 0 \tag{48}$$

Let us find f with a separation of variables as

$$f = u(r)v(\theta) \tag{49}$$

where u and v are functions of r and θ respectively.

Eq. (49) into Eq. (48) leads to,

$$A \left(\frac{r^2 v \partial^2 u}{\partial r^2} + \frac{u \partial^2 v}{\partial \theta^2} \right) - \frac{\partial^2 u}{\partial r^2} \frac{\partial^2 v}{\partial \theta^2} - r^2 C u v = 0 \tag{50}$$

where,

$$C = A^2 - 4B^2 \tag{51}$$

Eq. (50) becomes,

$$\frac{\partial^2 v}{\partial \theta^2}\left(\frac{A\partial^2 u}{\partial r^2} - u\right) = v\left(\frac{r^2 A\partial^2 u}{\partial r^2} - Cr^2 u\right) \qquad (52)$$

If,

$$\frac{A\partial^2 u}{\partial r^2} - u = 0 \qquad (53)$$

since neither of $\frac{\partial^2 v}{\partial \theta^2}$ and v can not be equal to zero, which implies,

$$\frac{r^2 A\partial^2 u}{\partial r^2} - Cr^2 u{=}0 \qquad (54)$$

and that imposes C to be equal to one, for all r different from zero, what is not truth.

Then,

$$\frac{\frac{\partial^2 v}{\partial \theta^2}}{v} = \frac{\frac{r^2 A\partial^2 u}{\partial r^2} - Cr^2 u}{\frac{A\partial^2 u}{\partial r^2} - u} = K \qquad (55)$$

where K is a real constant.

Eq. (55) implies that,

$$\frac{\partial^2 v}{\partial \theta^2} = Kv \tag{56}$$

If K is positive then the general solution of Eq. (56) will take the form of a linear combination of $e^{\sqrt{K}\theta}$ and $e^{-\sqrt{K}\theta}$. This solution causes problems with the mentioned boundary conditions because the incident beam at the reactor wall is a trigonometrical function of θ. Thus, K will be taken as zero or negatively, and the solutions of Eq. (56) are the family of the eigenfunctions v_K corresponding to the eigenvalues K defined as:

$$v_K = m_K cos\left(\sqrt{-K}\theta\right) + p_K sin\left(\sqrt{-K}\theta\right) \tag{57}$$

where m_K and p_K are real constants. The eigenvalues K are found considering that physically the specific intensity of the radiation G must be $2\pi -$periodic with respect to θ [44], then v_K should also be $2\pi -$periodic with respect to θ since G is a function of v_K. That means Eq.. 58 should be satisfied.

$$v_K(\theta + 2\pi) = v_K(\theta) \tag{58}$$

Eq. (58) implies $\sqrt{-K}$ should take the values $n = 0,1,2, ...$, then $K = -n^2, n = 0,1,2, ...$

Eq. (55) leads to,

$$\frac{\partial^2 u}{\partial r^2} = A \frac{n^2 + \frac{C}{A}r^2}{n^2 + Ar^2} u \tag{59}$$

Since u and v also depend on K and thus on n, they can be named u_n and v_n respectively. Eqs. (25-27), (44-45) and Eq. (51) show that $\frac{C}{A}$ and A all depend on the photon mean free path λ_0, the catalyst loading C_{cat}, its albedo ω, its scattering probabilities f, b, and s. For any value of the catalyst loading and any value of r in the interval [0; R], R the reactor radius, if $n \ll \frac{C}{A}r^2$, then $n \ll Ar^2$ since $\frac{C}{A} \leq A$

(see Eq. 51), thus $\frac{n^2+\frac{C}{A}r^2}{n^2+Ar^2} \approx \frac{C}{A^2}$; if $n \gg Ar^2$, then $n \gg \frac{C}{A}r^2$ since $\frac{C}{A} \leq A$, thus $\frac{n^2+\frac{C}{A}r^2}{n^2+Ar^2} \approx 1$; in all cases,

$\frac{n^2+\frac{C}{A}r^2}{n^2+Ar^2}$ does not vary too much. Then to simplify Eq. (59) one can replace $\frac{n^2+\frac{C}{A}r^2}{n^2+Ar^2}$ by its mean over

the interval [0, R] named α_n; then,

$$\alpha_n = \frac{1}{R}\int_0^R \left(\frac{n^2+\frac{C}{A}r^2}{n^2+Ar^2}\right) dr = \frac{C}{A^2} + \frac{4B^2n}{A^{\frac{5}{2}}R}\tan^{-1}\left(\frac{R\sqrt{A}}{n}\right) \tag{60}$$

Eq. (59) turns to,

$$\frac{\partial^2 u_n}{\partial r^2} = A\alpha_n u_n \tag{61}$$

which implies,

$$u_n = j_n e^{\sqrt{A\alpha_n}r} + l_n e^{-\sqrt{A\alpha_n}r} \tag{62}$$

where j_n and l_n are real constants. The general solution of the partial differential equation Eq. (57) is the superposition of the set of solutions (one must consider all eigenfunctions). Then using Eqs. (49), (56), and (62) f will take the general form,

$$f = \sum_{n=0}^{+\infty}\left[(m_n cos(n\theta) + p_n sin(n\theta))\left(j_n e^{\sqrt{A\alpha_n}r} + l_n e^{-\sqrt{A\alpha_n}r}\right)\right]$$ (63)

Combining Eqs. (46) and (63) results to,

$$g = \frac{A}{2Br}\sum_{n=0}^{+\infty}\left[(1-\alpha_n)(m_n cos(n\theta) + p_n sin(n\theta))\left(j_n e^{\sqrt{A\alpha_n}r} + l_n e^{-\sqrt{A\alpha_n}r}\right)\right]$$ (64)

(21) +(22), (23) +(24), (42) and (43) give,

$$\frac{\partial(f)}{\partial r} = -(C_1 + C_2)r(E_1 - E_2)$$ (65)

$$\frac{\partial(g)}{\partial r} = -(C_1 + C_2)r(E_3 - E_4)$$ (66)

Combining Eqs. (42) and (65) then Eqs. (43) and (66) respectively one finds:

$$E_1 = \frac{1}{2r}\left(f - \frac{1}{C_1+C_2}\frac{\partial(f)}{\partial r}\right)$$ (67)

$$E_2 = \frac{1}{2r}\left(f + \frac{1}{C_1+C_2}\frac{\partial(f)}{\partial r}\right)$$ (68)

$$E_3 = \frac{1}{2}\left(g - \frac{1}{C_1+C_2}\frac{\partial(g)}{\partial \theta}\right)$$ (69)

$$E_4 = \frac{1}{2}\left(g + \frac{1}{C_1+C_2}\frac{\partial(g)}{\partial \theta}\right)$$ (70)

Finally, combining Eqs. (67) and (63), Eqs. (68) and (63), Eqs. (69) and (64), Eqs. (70) and (64) respectively one finds:

$$E_1 = \frac{1}{2r}\sum_{n=0}^{+\infty}\left[v_n\left(j_n\left(1 - \frac{\sqrt{A\alpha_n}}{C_1+C_2}\right)e^{\sqrt{A\alpha_n}r} + l_n\left(1 + \frac{\sqrt{A\alpha_n}}{C_1+C_2}\right)e^{-\sqrt{A\alpha_n}r}\right)\right]$$ (71)

$$E_2 = \frac{1}{2r}\sum_{n=0}^{+\infty}\left[v_n\left(j_n\left(1 + \frac{\sqrt{A\alpha_n}}{C_1+C_2}\right)e^{\sqrt{A\alpha_n}r} + l_n\left(1 - \frac{\sqrt{A\alpha_n}}{C_1+C_2}\right)e^{-\sqrt{A\alpha_n}r}\right)\right]$$ (72)

$$E_3 = \frac{\zeta}{2r}\sum_{n=0}^{+\infty}\left[u_n(1-\alpha_n)\left(\left(m_n - \frac{p_n n}{C_1+C_2}\right)cos(n\theta) + \left(p_n + \frac{m_n n}{C_1+C_2}\right)sin(n\theta)\right)\right]$$ (73)

$$E_4 = \frac{\zeta}{2r}\sum_{n=0}^{+\infty}\left[u_n(1-\alpha_n)\left(\left(m_n + \frac{p_n n}{C_1+C_2}\right)cos(n\theta) + \left(p_n - \frac{m_n n}{C_1+C_2}\right)sin(n\theta)\right)\right]$$ (74)

where,

$$\zeta = \frac{A}{2B} \tag{75}$$

Introducing Eqs. (71-74) into Eq. (20), one finds,

$$E_5 = E_6 = \frac{\omega s \ \sum_{n=0}^{+\infty}\left[(1+\zeta(1-\alpha_n))(m_n cos(n\theta)+p_n sin(n\theta))\left(j_n e^{\sqrt{A\alpha_n}r}+l_n e^{-\sqrt{A\alpha_n}r}\right)\right]}{(1-\omega f-\omega b)r} \tag{76}$$

The specific intensity of the radiation G is equal to $\sum_{i=1}^{6} E_i$ which leads to,

$$G(r,\theta) = \frac{\zeta^* \sum_{n=0}^{+\infty}\left[(1+\zeta(1-\alpha_n))(m_n cos(n\theta)+p_n sin(n\theta))\left(j_n e^{\sqrt{A\alpha_n}r}+l_n e^{-\sqrt{A\alpha_n}r}\right)\right]}{r} \tag{77}$$

where,

$$\zeta^* = 1 + \frac{2\omega s}{(1-\omega f-\omega b)} \tag{78}$$

In terms of the angular variable, the expression of $G(r,\theta)$ is a Fourier series. The fact that G should not diverge when $r = 0$ leads to,

$$j_n + l_n = 0 \tag{79}$$

Eq. (79) into Eq. (77) implies,

$$G(r, \theta) = \frac{2\zeta^*}{r} \sum_{n=0}^{+\infty} \left[j_n (1 + \zeta(1 - \alpha_n)) \left(m_n cos(n\theta) + p_n sin(n\theta) \right) sinh\left(\sqrt{A\alpha_n} r \right) \right] \tag{80}$$

For the determination of the integration constants, it is necessary to expand the incident radiation reaching the reactor wall $G_0(R, \theta)$ as a Fourier series [44] as follows,

$$G_0(R, \theta) = \frac{h_0}{2} + \sum_{n=1}^{+\infty} [h_n cos(n\theta) + w_n sin(n\theta)] \tag{81}$$

where h_n and w_n are G_0 Fourier series expansion constants are defined by Eqs. (82-84) using the so-called orthogonality relations between sine and cosine functions.

$$h_0 = \frac{1}{\pi} \int_0^{2\pi} G_0(R, \theta) d\theta \tag{82}$$

$$h_n = \frac{1}{\pi} \int_0^{2\pi} G_0(R, \theta) cos(n\theta) d\theta \tag{83}$$

$$w_n = \frac{1}{\pi} \int_0^{2\pi} G_0(R, \theta) \sin(n\theta) d\theta \tag{84}$$

The $LVRPA$ will be defined as,

$$LVRPA(r, \theta) = (\kappa + \kappa_c) G(r, \theta) \tag{85}$$

where κ and κ_c are catalyst and contaminant absorption coefficients respectively.

7.2. Considerations at the boundary for the determination of integration constants

The constants of integration were modeled using the scheme shown in Figure 9. In this case, the incident beam I_0 will be considered coming parallel to the reactor axis. Applying Lambert's cosine law, for the upper hemicylindrical reactor tube,

$$G_0(R, \theta) = I_0 \cos\left(\frac{\pi}{2} - \theta\right) = I_0 \sin\theta \tag{86}$$

The following boundary condition should be considered,

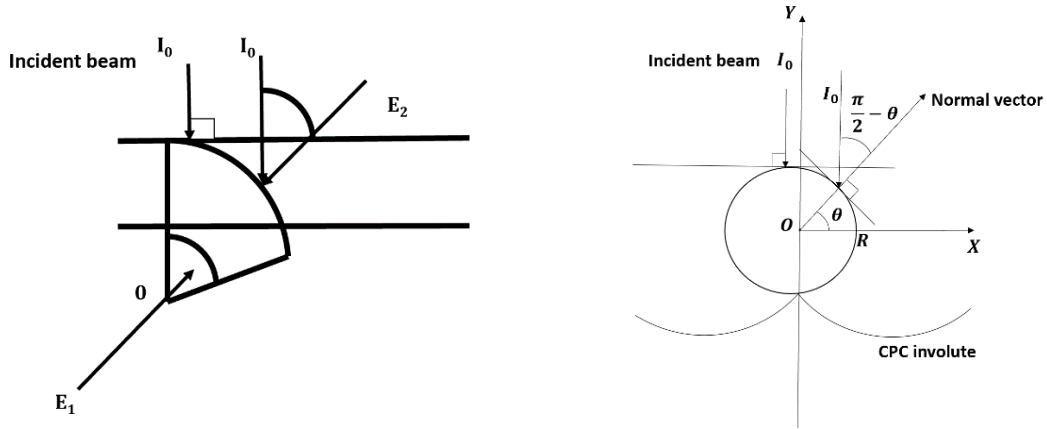$$G_0(R, \theta) = E_2(R, \theta). \tag{87}$$

Eqs. (72), (86), and (87) imply that

$$\frac{1}{2R} \sum_{n=0}^{+\infty} \left[j_n (m_n \cos(n\theta) + p_n \sin(n\theta)) \left(\left(1 + \frac{\sqrt{A\alpha_n}}{C_1 + C_2} \right) e^{\sqrt{A\alpha_n}R} - \left(1 - \frac{\sqrt{A\alpha_n}}{C_1 + C_2} \right) e^{-\sqrt{A\alpha_n}R} \right) \right] = I_0 \sin\theta \tag{88}$$

53

Eq. (88) implies that the unique coefficient in the E_2 Fourier series expansion which is not zero corresponds to $n = 1$. p_1 can be taken equal to unity and $m_1 = 0$, then,

$$j_1 = \frac{2RI_0}{\left(1+\frac{\sqrt{A\alpha_1}}{C_1+C_2}\right)e^{\sqrt{A\alpha_1}R}-\left(1-\frac{\sqrt{A\alpha_1}}{C_1+C_2}\right)e^{-\sqrt{A\alpha_1}R}} \tag{89}$$

where R is the reactor radius.

Fig. 9. Representation of boundary conditions for SFM-2D. a) Boundary representation of radiation entrance, b) Lambert's cosine law.

The $LVRPA$ for the upper side of the reactor tube $LVRPA^{sup}$ will be defined as

$$LVRPA^{sup}(r,\theta) = \frac{2R(\kappa+\kappa_c)\zeta^*I_0}{r}\frac{(1+\zeta(1-\alpha_1))\left(sinh(\sqrt{A\alpha_1}r)\right)sin\theta}{sinh(\sqrt{A\alpha_1}R)+\frac{\sqrt{A\alpha_1}}{C_1+C_2}cosh(\sqrt{A\alpha_1}R)} \tag{90}$$

Eq. 90 also represents the $LVRPA$ for a tubular reactor since it receives no radiation at its lower side.

To use the general solution Eq. (80) for the modeling of the lower hemicylindrical reactor tube, it is only necessary to obtain the distribution of the radiative flux on the reactor wall (See Equation Eq. (81)), say by applying the ray-tracing technique (See Figure 10) to the solar collector, and to expand the resulting distribution of radiative flux in a Fourier expansion [31].
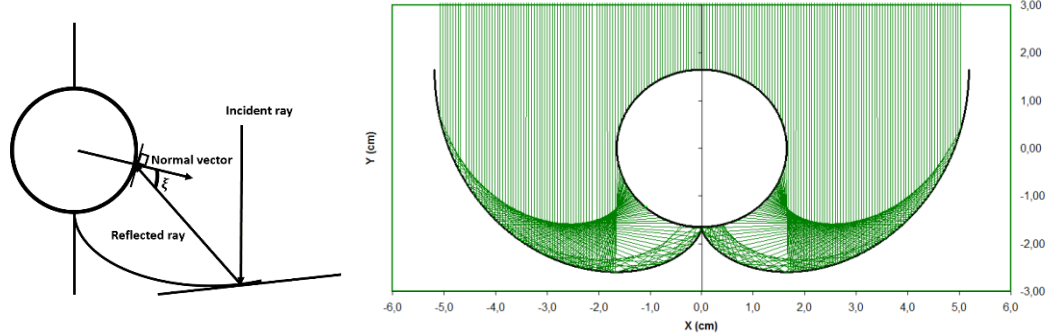
Fig. 10. Ray Tracing Technique applied on the CPC: a) Incident angle ξ, b) Simulation on CPC

Let's a define $G_0(R, \theta)$ as a $2\pi -$periodic function with respect to θ as follows,

$$G_0(R, \theta) = \begin{cases} 0, & if\ \theta \in [0; \pi] - \{\pi\} \\ I_0 \psi^N cos(\xi), & if\ \theta \in [\pi; 2\pi] \end{cases} \tag{91}$$

where ψ is the reflectivity of the CPC reflectors and N is the average number of consecutive reflections of a given ray on the CPC reflector before reaching the tube, ξ is the average incidence angle that forms the incoming radiation with the normal vector at a given point where the ray hits the reactor tube. In our future works, the investigation related to the exact value of ξ will be taken into account since it has not been reported in the literature. In this work, ξ was taken $\frac{\pi}{4}$ only for the simulation.

Using Eqs. (81) and (91), the $G_0(R, \theta)$ Fourier series expansion coefficients are,

$$h_0 = \frac{1}{\pi} \int_0^{2\pi} G_0(R, \theta) d\theta = I_0 \psi^N \cos(\xi) \tag{92}$$

$$h_n = \frac{1}{\pi} \int_0^{2\pi} G_0(R, \theta) \cos(n\theta) d\theta = 0 \tag{93}$$

$$w_n = \frac{1}{\pi} \int_0^{2\pi} G_0(R, \theta) \sin(n\theta) d\theta = \frac{I_0 \psi^N \cos(\xi)(-1+\cos(n\pi))}{n\pi} \tag{94}$$

Using Eq. (72), and Eq. (79) and applying the boundary condition Eq. (87), one finds, $m_n = 0$, $p_n = 1$,

$$j_0 = \frac{R I_0 \psi^N \cos(\xi)}{\left(1+\frac{\sqrt{A\alpha_0}}{C_1+C_2}\right)e^{\sqrt{A\alpha_0}R} - \left(1-\frac{\sqrt{A\alpha_0}}{C_1+C_2}\right)e^{-\sqrt{A\alpha_0}R}} = \frac{R I_0 \psi^N \cos(\xi)}{2\left(\sinh(\sqrt{A\alpha_0}R) + \frac{\sqrt{A\alpha_0}}{C_1+C_2}\cosh(\sqrt{A\alpha_0}R)\right)} \tag{95}$$

For $n > 0$,

$$j_n = \frac{1}{n\pi} \frac{2 R I_0 \psi^N \cos(\xi)(-1+\cos(n\pi))}{\left(1+\frac{\sqrt{A\alpha_n}}{C_1+C_2}\right)e^{\sqrt{A\alpha_n}R} - \left(1-\frac{\sqrt{A\alpha_n}}{C_1+C_2}\right)e^{-\sqrt{A\alpha_n}R}} = \frac{1}{n\pi} \frac{R I_0 \psi^N \cos(\xi)(-1+(-1)^n)}{\sinh(\sqrt{A\alpha_n}R) + \frac{\sqrt{A\alpha_n}}{C_1+C_2}\cosh(\sqrt{A\alpha_n}R)} \tag{96}$$

Eq. (95) and Eq. (96) into Eq. (80) give the specific intensity of the radiation $G(r, \theta)$ as,

$$G(r, \theta) = \frac{2\zeta^* R I_0 \psi^N \cos(\xi)}{r} \left(\frac{(1+\zeta(1-\alpha_0))\sinh(\sqrt{A\alpha_0}r)}{2\left(\sinh(\sqrt{A\alpha_0}R) + \frac{\sqrt{A\alpha_0}}{C_1+C_2}\cosh(\sqrt{A\alpha_0}R)\right)} + \sum_{n=1}^{+\infty}\left[\frac{(-1+(-1)^n)}{n\pi}\frac{(1+\zeta(1-\alpha_n))(\sin(n\theta))\sinh(\sqrt{A\alpha_n}r)}{\sinh(\sqrt{A\alpha_n}R) + \frac{\sqrt{A\alpha_n}}{C_1+C_2}\cosh(\sqrt{A\alpha_n}R)}\right] \right) \tag{97}$$

and the $LVRPA$ for the lower side of the reactor tube, $LVRPA^{inf}$ is,

$$LVRPA^{inf} = \frac{2\zeta^*(\kappa+\kappa_c)RI_0\psi^N cos(\xi)}{r}\left(\frac{(1+\zeta(1-\alpha_0))sinh(\sqrt{A\alpha_0}r)}{2\left(sinh(\sqrt{A\alpha_0}R)+\frac{\sqrt{A\alpha_0}}{C_1+C_2}cosh(\sqrt{A\alpha_0}R)\right)} + \sum_{n=1}^{+\infty}\left[\frac{(-1+(-1)^n)}{n\pi}\frac{(1+\zeta(1-\alpha_n))(sin(n\theta))sinh(\sqrt{A\alpha_n}r)}{sinh(\sqrt{A\alpha_n}R)+\frac{\sqrt{A\alpha_n}}{C_1+C_2}cosh(\sqrt{A\alpha_n}R)}\right]\right) \tag{98}$$

Eq. (98) will be evaluated for a finite term of the sum (10^6+1 for example).

Considering Lambert's cosine law in the boundary conditions, the $LVRPA$ for the entire CPC will be defined as,

$$LVRPA = \begin{cases} \frac{2R(\kappa+\kappa_c)\zeta^*I_0}{r}\frac{(1+\zeta(1-\alpha_1))\left(sinh(\sqrt{A\alpha_1}r)\right)sin\theta}{sinh(\sqrt{A\alpha_1}R)+\frac{\sqrt{A\alpha_1}}{C_1+C_2}cosh(\sqrt{A\alpha_1}R)}, & if\ \theta \in [0;\pi] \\ \\ \frac{2\zeta^*(\kappa+\kappa_c)RI_0\psi^N\left(\frac{(1+\zeta(1-\alpha_0))sinh(\sqrt{A\alpha_0}r)}{2\left(sinh(\sqrt{A\alpha_0}R)+\frac{\sqrt{A\alpha_0}}{C_1+C_2}cosh(\sqrt{A\alpha_0}R)\right)}+\sum_{n=1}^{+\infty}\left[\frac{(-1+(-1)^n)(1+\zeta(1-\alpha_n))(sin(n\theta))sinh(\sqrt{A\alpha_n}r)}{n\pi\ sinh(\sqrt{A\alpha_n}R)+\frac{\sqrt{A\alpha_n}}{C_1+C_2}cosh(\sqrt{A\alpha_n}R)}\right]\right)cos(\xi)}{r}, & if\ \theta \in [\pi;2\pi] \end{cases} \tag{99}$$

Without considering Lambert's cosine law in the boundary conditions, the incident radiation reaching the reactor wall $G_0(R,\theta)$ (for the upper side of the reactor) will be defined as a $2\pi -$periodic function with respect to θ as follows,

$$G_0(R,\theta) = \begin{cases} I_0, & if\ \theta \in [0;\pi] \\ 0, & if\ \theta \in [\pi;2\pi]-\{\pi\} \end{cases} \tag{100}$$

Using Eqs. (81) and (91), the $G_0(R,\theta)$ Fourier series expansion coefficients are,

$$h_0 = \frac{1}{\pi}\int_0^{2\pi} G_0(R,\theta)d\theta = I_0 \tag{101}$$

$$h_n = \frac{1}{\pi}\int_0^{2\pi} G_0(R,\theta)cos(n\theta)d\theta = 0 \tag{102}$$

$$w_n = \frac{1}{\pi}\int_0^{2\pi} G_0(R,\theta)sin(n\theta)d\theta = \frac{I_0(1-cos(n\pi))}{n\pi} \tag{103}$$

Using Eqs. (72), (79), and applying the boundary condition Eq. (87), one finds, $m_n = 0$, $p_n = 1$,

$$j_0 = \frac{RI_0}{\left(1+\frac{\sqrt{A\alpha_0}}{C_1+C_2}\right)e^{\sqrt{A\alpha_0}R}-\left(1-\frac{\sqrt{A\alpha_0}}{C_1+C_2}\right)e^{-\sqrt{A\alpha_0}R}} = \frac{RI_0}{2\left(sinh(\sqrt{A\alpha_0}R)+\frac{\sqrt{A\alpha_0}}{C_1+C_2}cosh(\sqrt{A\alpha_0}R)\right)} \tag{104}$$

For $n > 0$,

$$j_n = \frac{1}{n\pi}\frac{2RI_0(1-cos(n\pi))}{\left(1+\frac{\sqrt{A\alpha_n}}{C_1+C_2}\right)e^{\sqrt{A\alpha_n}R}-\left(1-\frac{\sqrt{A\alpha_n}}{C_1+C_2}\right)e^{-\sqrt{A\alpha_n}R}} = \frac{1}{n\pi}\frac{RI_0(1-(-1)^n)}{sinh(\sqrt{A\alpha_n}R)+\frac{\sqrt{A\alpha_n}}{C_1+C_2}cosh(\sqrt{A\alpha_n}R)} \tag{105}$$

Eqs. (104) and (105) into (80) give the specific intensity of the radiation $G(r,\theta)$ as,

$$G(r,\theta) = \frac{2\zeta^* RI_0}{r}\left(\frac{(1+\zeta(1-\alpha_0))sinh(\sqrt{A\alpha_0}r)}{2\left(sinh(\sqrt{A\alpha_0}R)+\frac{\sqrt{A\alpha_0}}{C_1+C_2}cosh(\sqrt{A\alpha_0}R)\right)} + \sum_{n=1}^{+\infty}\left[\frac{(1-(-1)^n)}{n\pi}\frac{(1+\zeta(1-\alpha_n))(sin(n\theta))sinh(\sqrt{A\alpha_n}r)}{sinh(\sqrt{A\alpha_n}R)+\frac{\sqrt{A\alpha_n}}{C_1+C_2}cosh(\sqrt{A\alpha_n}R)}\right]\right) \tag{106}$$

and the $LVRPA$ for the upper side of the reactor tube, $LVRPA^{sup}$ is,

$$LVRPA^{sup} = \frac{2\zeta^*(\kappa+\kappa_c)RI_0}{r}\left(\frac{(1+\zeta(1-\alpha_0))sinh(\sqrt{A\alpha_0}r)}{2\left(sinh(\sqrt{A\alpha_0}R)+\frac{\sqrt{A\alpha_0}}{C_1+C_2}cosh(\sqrt{A\alpha_0}R)\right)} + \sum_{n=1}^{+\infty}\left[\frac{(1-(-1)^n)}{n\pi}\frac{(1+\zeta(1-\alpha_n))(sin(n\theta))sinh(\sqrt{A\alpha_n}r)}{sinh(\sqrt{A\alpha_n}R)+\frac{\sqrt{A\alpha_n}}{C_1+C_2}cosh(\sqrt{A\alpha_n}R)}\right]\right) \tag{107}$$

Eq. (107) also represents the $LVRPA$ for a tubular reactor since it receives no radiation at its lower side.

For the lower side of the CPC reactor, the $LVRPA$ is found by replacing $cos(\xi)$ by unity in Eq. (99). Then omitting Lambert's cosine law in the boundary conditions, the $LVRPA$ for the entire CPC will be defined as,

$$LVRPA = \begin{cases} \frac{2\zeta^*(\kappa+\kappa_c)RI_0}{r}\left(\frac{(1+\zeta(1-\alpha_0))sinh(\sqrt{A\alpha_0}r)}{2\left(sinh(\sqrt{A\alpha_0}R)+\frac{\sqrt{A\alpha_0}}{C_1+C_2}cosh(\sqrt{A\alpha_0}R)\right)}+\sum_{n=1}^{+\infty}\left[\frac{(1-(-1)^n)}{n\pi}\frac{(1+\zeta(1-\alpha_n))(sin(n\theta))sinh(\sqrt{A\alpha_n}r)}{sinh(\sqrt{A\alpha_n}R)+\frac{\sqrt{A\alpha_n}}{C_1+C_2}cosh(\sqrt{A\alpha_n}R)}\right]\right), & if\ \theta \in [0;\pi] \\[2em] \frac{2\zeta^*(\kappa+\kappa_c)RI_0\psi^N}{r}\left(\frac{(1+\zeta(1-\alpha_0))sinh(\sqrt{A\alpha_0}r)}{2\left(sinh(\sqrt{A\alpha_0}R)+\frac{\sqrt{A\alpha_0}}{C_1+C_2}cosh(\sqrt{A\alpha_0}R)\right)}+\sum_{n=1}^{+\infty}\left[\frac{(-1+(-1)^n)}{n\pi}\frac{(1+\zeta(1-\alpha_n))(sin(n\theta))sinh(\sqrt{A\alpha_n}r)}{sinh(\sqrt{A\alpha_n}R)+\frac{\sqrt{A\alpha_n}}{C_1+C_2}cosh(\sqrt{A\alpha_n}R)}\right]\right), & if\ \theta \in [\pi;2\pi] \end{cases} \tag{108}$$

The volumetric rate of photon absorption per unit reactor length, $VRPA/H$, which describes the distribution of the photon absorption inside the reactor, is defined in Eqs. (109–110) for both sides of the reactor tube, gives a broader view of the energy absorption since it does not depend on the reactor length. The overall volumetric rate of photon absorption (OVRPA) is obtained just by multiplying the $VRPA/H$ by the reactor length.

$$VRPA^{sup}/H = \int_0^R \int_0^\pi LVRPA\,r\,dr\,d\theta \tag{109}$$

$$VRPA^{inf}/H = \int_0^R \int_\pi^{2\pi} LVRPA\,r\,dr\,d\theta \tag{110}$$

$$VRPA^{sup}/H = \frac{4R(\kappa+\kappa_c)I_0\zeta^*}{\sqrt{A\alpha_1}}\frac{(1+\zeta(1-\alpha_1))(cosh(\sqrt{A\alpha_1}R)-1)}{sinh(\sqrt{A\alpha_1}R)+\frac{\sqrt{A\alpha_1}}{C_1+C_2}cosh(\sqrt{A\alpha_1}R)} \tag{111}$$

$$VRPA^{inf}/H = 2(\kappa+\kappa_c)RI_0\psi^N cos(\xi)\zeta^*\left(\frac{\pi(1+\zeta(1-\alpha_0))cosh(\sqrt{A\alpha_0}R)}{2\sqrt{A\alpha_0}\left(sinh(\sqrt{A\alpha_0}R)+\frac{\sqrt{A\alpha_0}}{C_1+C_2}cosh(\sqrt{A\alpha_0}R)\right)}+\sum_{n=1}^{+\infty}\left[\frac{(-1+(-1)^n)^2(1+\zeta(1-\alpha_n))(cosh(\sqrt{A\alpha_n}R)-1)}{n^2\pi\sqrt{A\alpha_n}\left(sinh(\sqrt{A\alpha_n}R)+\frac{\sqrt{A\alpha_n}}{C_1+C_2}cosh(\sqrt{A\alpha_n}R)\right)}\right]\right) \tag{112}$$

For the entire CPC and considering Lambert's cosine law in the boundary conditions,

$$VRPA/H = VRPA^{sup}/H + VRPA^{inf}/H \qquad (113)$$

The same procedure is used to calculate the $VRPA/H$ for the entire CPC for the case of not considering Lambert's cosine law in the boundary conditions using equations Eqs. (109), (110), and (113).

Note that N can be calculated using Eq. (114) (Rabl et al. 1979).

$$N = 1 + 0.07 * C_{cpc} \qquad (114)$$

where C_{cpc} is the concentrator ratio of the CPC which is calculated as,

$$C_{cpc} = \frac{1}{sin(\theta_{cpc})} \qquad (115)$$

where θ_{cpc} is the half acceptance angle of the CPC.

7.3. Modeling for the estimation of the catalyst optical properties

The determination of the optical catalyst properties has been a challenging and complicated task since one should deal with the RTE and there are only a few works regarding that in the literature (Cabrera et al., 1996; Satuf et al., 2005). Usually, the determination of the extinction coefficient is not

complicated since it is related to the absorbance (Cabrera et al. (1996); Satuf et al. (2005)), which can be easily measured using a spectrophotometer UV-Vis. Getting the extinction coefficient does not give information about absorption in a defined medium, so it is mandatory to perform a supplementary experiment to find either the absorption or scattering coefficient. It is worth mentioning that the sum of both coefficients gives the extinction coefficient. An independent measurement can be obtained by using the cell space total diffuse reflectance accessory (CSTDR accessory) of the Cary 17 spectrophotometer, but unfortunately, this equipment was not available when implementing this work. The method used in this work was to follow the SFM-1D approach to solve the RTE and then express the transmittance (T_λ) as a function of the catalyst optical properties and scattering probabilities at each wavelength λ in the UV radiation spectrum interval [295;405] nm. Then the experimental transmittance T_λ^{Exp} of the solid suspensions was measured for five different catalyst concentrations (0.01, 0.03, 0.05, 0.07, and 0.1 g/L) at 12 different wavelengths from 295 to 405 nm in equally separated intervals of 10 nm. The scattering probabilities at each wavelength λ are expressed using Eq. (1-3) proposed by Chu and Churchill (1956) using the HG phase function defined in Eq. (116) (the SFM-1D was already defined earlier in this work).

$$\phi(\theta) = \frac{\omega}{4\pi} \frac{1-g^2}{(1+g^2-2g\cos\theta)^{\frac{3}{2}}} \tag{116}$$

$$\omega = 2\pi \int_0^\pi \phi(\theta) \sin\theta \, d\theta = \frac{\sigma}{\sigma+\kappa} \tag{117}$$

$$f = 2\pi \int_0^{\frac{\pi}{2}} \phi(\theta) (\cos\theta)^2 \sin\theta \, d\theta = \frac{\omega(1-g^2)\left(\frac{3g^2}{1-g}+6g(1-g)+2(1-g)^3-2(1+g^2)^{\frac{3}{2}}\right)}{6g^3} \tag{118}$$

$$b = 2\pi \int_{\frac{\pi}{2}}^{\pi} \phi(\theta) \, (\cos\theta)^2 \sin\theta \, d\theta \;\; = \frac{\omega(1-g^2)\left(\frac{-3g^2}{1+g}+6g(1+g)-2(1+g)^3+2\left(1+g^2\right)^{\frac{3}{2}}\right)}{6g^3} \tag{119}$$

$$s = \frac{1}{4}(1 - f - b) = \frac{1}{4}\left(1 - \frac{\omega}{3}(1 + 2g^2)\right) \tag{120}$$

where $\phi(\theta)$, θ and g are respectively the HG phase function, the scattering angle, and the asymmetry factor, which takes the values from -1(if it is a pure backward scattering) to 1(if it is a pure forward scattering). The value 0 corresponds to isotropic scattering. The other parameters were defined in this investigation. Figure 11 shows the behavior of these probabilities as a function of different values of ω.

a)   **b)**
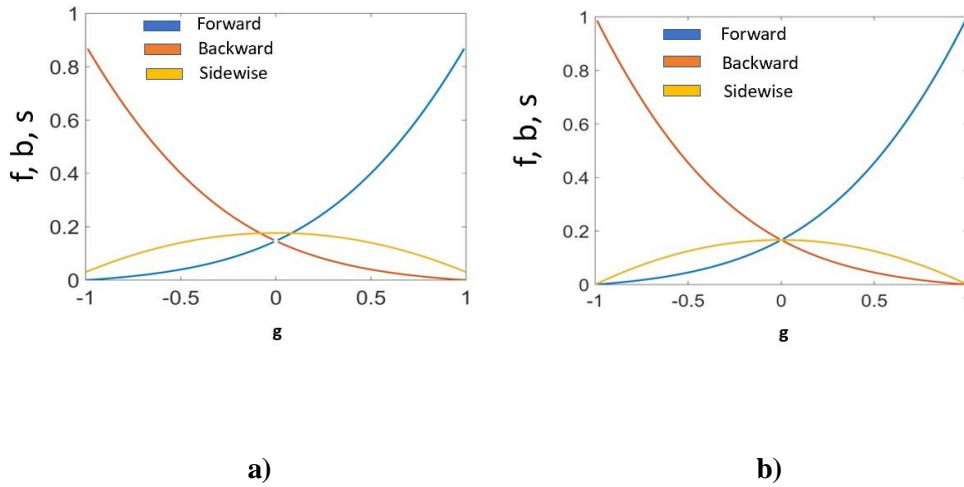
Figure. 11. Forward (blue line), backward (Orange line), and sidewise (yellow line) scattering probability vs the asymmetric factor with two different scattering albedo.

a) Scattering albedo ω equal to 0.88   b) Scattering albedo ω equal to 1.

The SFM-1D was used to solve the RTE in a slab cell of length L (L =1cm) receiving light parallel to the plan XZ with the intensity $I_{0,\lambda}$ as depicted in Figure 12.
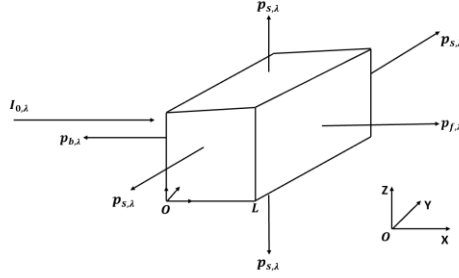
Fig. 12. The SFM-1D in slab cell of length L.

The SFM-1D parameters were rewritten for each wavelength λ, as well as the reflectance and transmittance fluxes (A. Brucato et al., 2006) from Eqs. (121-128) as follows:

$$a_\lambda = 1 - \omega_\lambda p_{f,\lambda} - \frac{4\left(\omega_\lambda p_{s,\lambda}\right)^2}{\left(1 - \omega_\lambda p_{f,\lambda} - \omega_\lambda p_{b,\lambda} - 2\omega_\lambda p_{s,\lambda}\right)} \tag{121}$$

$$b_\lambda = \omega_\lambda p_{b,\lambda} + \frac{4\left(\omega_\lambda p_s\right)^2}{\left(1 - \omega_\lambda p_{f,\lambda} - \omega_\lambda p_{b,\lambda} - 2\omega_\lambda p_{s,\lambda}\right)} \tag{122}$$

$$\omega_{corr} = \frac{b_\lambda}{a_\lambda} \tag{123}$$

$$\lambda_0 = \frac{1}{(\sigma_\lambda + \kappa_\lambda)c_{cat}} = \frac{1}{\beta_\lambda} \tag{124}$$

$$\lambda_{\omega_{corr}} = \frac{\lambda_0}{a_\lambda \sqrt{1-(\omega_{corr})^2}} \tag{125}$$

$$\gamma = \frac{1-\sqrt{1-(\omega_{corr})^2}}{1+\sqrt{1-(\omega_{corr})^2}} e^{-\frac{2L}{\lambda_{\omega_{corr}}}} \tag{126}$$

$$T_\lambda = \frac{1}{1-\gamma} \frac{2\sqrt{1-(\omega_{corr})^2}}{1+\sqrt{1-(\omega_{corr})^2}} e^{-\frac{L}{\lambda_{\omega_{corr}}}} \tag{127}$$

$$R_\lambda = \frac{1}{\omega_{corr}} \left(1 - \frac{1+\gamma}{1-\gamma}\sqrt{1-(\omega_{corr})^2}\right) \tag{128}$$

where $p_{f,\lambda}$, $p_{b,\lambda}$ and $p_{s,\lambda}$ represent the forward, backward, and sidewise probabilities at wavelength λ respectively. Eq. (128) gives the value of the reflectance R_λ.

Then, minimizing the difference between the theoretical and experimental value of the transmittance in such a way that $\left|T_\lambda - T_\lambda^{Exp}\right| \leq 10^{-n}$, where $n \geq 3$ is an integer, the catalyst

asymmetric factor g_λ and albedo ω_λ were easily found for each wavelength λ. Since β_λ is known already, σ_λ and κ_λ are deduced. This procedure was adopted for the flesh and the used catalyst as well as for each cycle of the catalyst reuse. A mathematical relation was established between each of the catalyst properties and the order of the cycle of the catalyst reuse.

7. 4. Kinetic model and mass balance

Numerous studies have shown that the photocatalytic degradation of emerging pharmaceutical contaminants and principally of SMX follows pseudo-first-order kinetics [45] and an apparent Langmuir-Hinshelwood (L-H) rate equation. To determine kinetic parameters independent of reactor geometry and radiation field, the L-H's rate law should include a high dependency on photon flux, represented by the LVRPA [13] as follows:

$$-r_C = k \sqrt{\frac{OVRPA}{v_R}} \frac{KC}{1+KC} \tag{129}$$

where k and K represent the kinetic constant and the binding constant associated with the adsorption of SMX on the catalyst surface, respectively; v_R (m^3) and C (ppm) are the reactor volume (illuminated reaction zone) and the SMX concentration, respectively, r_C (ppm/min) is the SMX degradation rate.

When the substrate concentration is lower than 10^{-3} mol/L, as is the case in this work, Eq. (129) can be reduced to [46]:

$$-r_C = k_{app}C, \; k_{app} = kK\sqrt{\frac{OVRPA}{v_R}} \tag{130}$$

k_{app} (1/min) is associated with the SMX adsorption behavior, the photon absorption and the SMX kinetic constant and $k_p = kK$ ($W^{0.5}m^{-1.5}$min) with SMX adsorption behavior and the SMX kinetic constant. The mass balance equation for the solar reactor in the reaction zone (illuminated zone) is [13]:

$$\frac{\partial C}{\partial t_{30W}} = \frac{v_R}{v_T}r_C \tag{131}$$

where v_T is the total reaction volume (illuminated and dark reaction zone). The standardized time t_{30W} (minutes) is well defined later in this work.

The integration of Eq. (131) gives:

$$\ln\frac{C}{C_0} = -k_{app}\frac{v_R}{v_T}t_{30W} \tag{132}$$

where C_0 is the SMX initial concentration.

The kinetic model for the degradation of the SMX considering the catalyst reuse will be defined as follows:

$$\ln\frac{C_n}{C_0} = -k_{app,n}\frac{v_R}{v_T}t_{30W} \tag{133}$$

where C_n, $k_{app,n} = k_n K_n \sqrt{\dfrac{\text{OVRPA}_n}{v_R}}$, k_n and K_n are the SMX concentration, the apparent kinetic, the

kinetic, and the adsorption coefficients respectively for the nth reuse. OVRPA_n represents the OVRPA

for the nth reuse and $k_{p,n} = k_n K_n$.

8. Experimental

Chemical

SMX ($C_{10}H_{11}N_3O_3S$) was supplied by Sigma-Aldrich. The heterogeneous photocatalytic degradation

tests were carried out using a slurry solution of Degussa (Frankfurt, Germany) P-25 titanium dioxide

(primary particle size, 20-30 nm; specific surface area 61 m^2/g by BET; composition 75 % anatase

and 25 % rutile by X-ray diffraction, bandgap, 3.35 eV).

Analytical determinations

SMX was analyzed using reverse-phase liquid chromatography (at 0.5 ml/min) with UV detection in

an HPLC-UV (Young Lin, YL 9100) with a C-18 column (LUNA 5 mm, 250 ´ 4.6 mm from

Phenomenex). Total organic carbon (TOC) was analyzed by direct injection of the filtered samples

into a Shimadzu TOC analyzer (TOC-VCSH). The spectrophotometer UV-Vis (Varian, Cary 50) was

used for the measurement of absorbance.

Characterization techniques

The determination of the catalyst specific surface area was performed from the nitrogen adsorption-

desorption isotherms using the Brunauer–Emmett–Teller (BET) method based on data obtained from

the N_2 adsorption isotherm measured in a Micromeritics model TriStar II Plus device. The distribution

and the size of the pores were determined using the BJH (Barrett-Joyner-Halenda) method and DFT

for metal oxides. Catalyst samples were previously degassed under vacuum at a temperature of 120

°C for 2 h before being analyzed. The catalyst band gap (Eg) was analyzed by spectroscopy of diffuse

UV-Vis reflectance (DRS) with a Perkin Elmer UV-Vis spectrophotometer Lambda 365 model, in the range of 200 to 700 nm with dual beam and the accessory was used with a sweep rate of 300 nm per min.

The waste generated during the execution of the project will be disposed of and classified according to the regulations described by the Department of Waste Management and Control of the Faculty of Chemical Sciences of the Autonomous University of Nuevo León.

Materials and Methods

All the experiments were carried out under partly cloudy and sunny weather conditions in the CPC situated at the Laboratory of Photocatalysis and Environmental Electrochemistry in the School of Chemical Sciences (UANL) (N25 ° 41'30.3 "; W100 ° 18'34.9") in Monterrey (Mexico) during January and February 2022. The pilot-scale reactor is made up of a tank (10 L) and a pump. The CPC consists of five Pyrex tubes (but only two tubes were used for the experiments in this case) connected in series and mounted on a fixed platform tilted at 25 ° (local latitude). The water flows at 36 L/min (this flow rate is to ensure turbulent flow to facilitate the mass transfer in the reactor) directly from the module and finally into a tank. The total volume (V_T) of the reactor (10 L) is separated into two parts: 7.124 L of total irradiated volume (in Pyrex tubes) (V_i) and the dead reactor volume (tank + connecting tubes). The inner diameter and the length of the reactor tubes are 5.5 and 150 cm, respectively. At the beginning of the experiments, the collector was covered for 30 minutes to approach adsorption equilibrium between the substrate, the solid catalyst, and the walls of the apparatus. With the collector covered, all the chemicals were added to the tank and mixed until a constant concentration was achieved throughout the system. Then the cover was removed to initiate the photocatalytic degradation of the SMX solution. Samples were collected at predetermined times (t = 30 minutes), filtered through a 0.45 μm Nylon Millipore filter, and analyzed for the determination of the pollutant concentration and TOC determination. The initial pH of the SMX solution was

measured and found 6.19. The catalyst was recovered by sedimentation and filtration (Whatman, paper filter 2.5 μm) and then was dried in the oven for one day at 80 $^{\circ}$ C. A UV radiometer (KIPP & ZONEN, model CUV3) positioned on a platform tilted 25 $^{\circ}$ (the same angle as the CPC) recorded the solar ultraviolet radiation (UV), which provided data in terms of incident W_{uv} m^2. This value indicates the energy that can reach a surface while it is in the same location as the sun. The collection of the data from several days of experiments and their comparison with other solar photocatalytic experiments is possible using Eq. (134).

$$t_{30\,W,n} = t_{30\,W,n-1} + \Delta t_n \frac{\text{UV}}{30}\frac{V_i}{V_T};\ \Delta t_n = t_n - t_{n-1} \tag{134}$$

where t_n is the interval of time between two samples, UV is the average solar radiation intensity measured during Δt_n, and t$_{30w}$ is a ''standardized irradiation time''. In this case, time refers to a constant solar UV power of 30 W/m^2 (radiation flux intensity around noon on a perfect sunny day). When this simplification is used, the illumination time calculated by this procedure can be called t$_{30w}$. Q_{UV}. The amount of energy collected by the reactor (per unit of volume) from the start-up of the experiments until each sampling can be computed by Eq. (135) as:

$$Q_{\text{UV},n} = Q_{\text{UV},n-1} + \Delta t_n \text{UV}\frac{A_R}{V_T};\ \Delta t_n = t_n - t_{n-1} \tag{135}$$

where A_R is the radiation collecting surface of the photoreactor and $Q_{UV,n}$ is the cumulated energy (per unit of volume, kJ L^{-1}) having entered the reactor for each sample taken during the experiment. Sometimes it is useful (for those readers not interested in solar energy) to explain the results in terms of illumination time instead of Q_{UV}, as is the case in this work.

Solar photocatalytic degradation of 10 ppm of SMX in distilled water with different catalyst loadings (0.1, 0.2, 0.3, 0.4, and 0.5 g/L) was carried out in the CPC reactor under the same operating conditions. Then the catalyst loading, which led to the highest degradation, was chosen to perform five other experiments under the same operating conditions as previously but reusing the catalyst. After each experiment, the catalyst was recovered by sedimentation and filtration; the surface area, the bandgap, and the absorbance of the catalyst were measured. The specific extinction coefficients of the fresh, the used, and the reused catalysts were found using the method proposed by Satuf et al. (2005), as were the corresponding specific absorption and scattering catalyst coefficients. Then those catalyst properties cited above were introduced into the LVRPA and the OVRPA. Then the LVRPA was introduced into the kinetic model, and after performing the mass balance, the kinetic constants were determined using data collected from the different experiments.

9. Results and discussion

9. 1. Radiant field and application of the SFM-2D

The model presented here was the model to a CPC reactor (see Figure 13) at the Faculty of Chemical Sciences of the UANL (Mexico). Simulations were run using the following parameters:

Tube radius: R (m)	0.0165
Material	Duran borosilicate glass
Acceptance angle	90° (non-concentrating)
Reflexivity of the collector Surface	0.85
The solar UV radiation flux: I_0 (W/m^2)	30
The specific mass absorption coefficient κ^* (m^2/kg)	174.75
The specific mass scattering coefficient σ^*(m^2/kg)	1295.75
The specific mass absorption coefficient of a given contaminant: κ_c^*	Considered here equal to zero
The catalyst loading: C_{cat}(g/l)	Starting from zero g/l
The photon mean free path length: λ_0 (m)	$\dfrac{1}{\lambda_0} = (\sigma^* + \kappa^*)C_{cat} + \kappa_c^* C_c$
The scattering albedo ω: $\dfrac{\sigma^* C_{cat}}{(\sigma^* + \kappa^*)C_{cat} + \kappa_c^* C_c}$	0.88
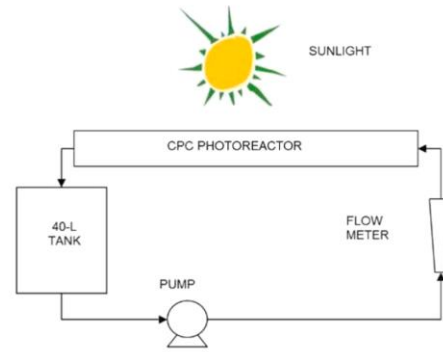
Fig. 13. Photocatalytic Solar CPC Reactor, UANL.

This model was simulated with an incident radiation intensity (I_0) of 30 W/m^2, which is the average value of the incident radiation flux on a clear sunny day [47, 48]. For our computations, we also used Lambert's cosine law (see Figure 9). We compared our results with other previous studies by carrying out simulations without considering Lambert's cosine law since most of the researchers neglected this law. Nonetheless, the results showed that the cosine Lambert law provides a very close approximation of the radiant field and a closer approximation than the SFM solved without considering this law [40]. Fig. 14 shows the VRPA/H for a CPC (CPC-DR-L, CPC-DR, CPC-HG-L, CPC-HG, solid line) and a tubular reactor (Tub-DR-L, Tub-DR, Tub-DR, Tub-HG-L, Tub-HG, dotted line) at different catalyst loadings with the DR and HG phase functions with the cases considering and not considering Lambert's cosine law.

a)   b)
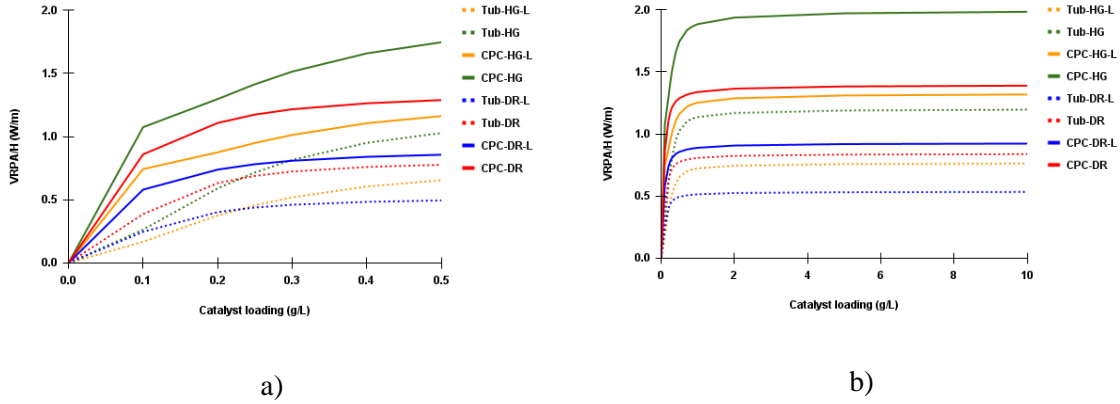
Fig. 14. Volumetric Rate of Photon Absorption per unit reactor length VRPA/H for a CPC (solid line) and a tubular reactor (dotted line) as a function of catalyst loading with the HG and DR phase functions with the cases considering and not considering Lambert's cosine law:

a) $0 \leq TiO_2\text{-}P25 \leq 0.5$ g/L, b) $0 \leq TiO_2\text{-}P25 \leq 10$ g/L

Furthermore, we compared the radiant field in tubular and CPC photoreactors using the SFM-2D, considering the diffuse reflectance (SFM-2D-DR) and Henyey-Greenstein phase functions (SFM-2D-HG). The SFM-2D's primary goal is to clear up the computation of VRPA/H in tubular and CPC reactors. The estimation of the VRPA/H using the SFM-1D adapted to tubular and CPC reactors [13, 31] was not accurately performed since it depends on the number of solar rays chosen for the discretization of the cross-section area of the reactor. As you increase the number of sun rays, the VRPA/H gets higher. Under the same operating conditions, Colina-Márquez et al. [13] discovered the VRPA/H at about 0.4 W/m using the SFM-1D-DR, while Acosta-Herazo et al. [31] found 1.12 and 1.45 W/m using the SFM-1D-DR and SFM-1D-HG, respectively. Using Lambert's cosine law, the computed VRPA/H for the SFM-2D-DR and SFM-2D-HG, respectively, at the same working conditions as Colina-Márquez et al. and Acosta-Herazo et al. [13, 31] was 0.52 and 1.01 W/m, respectively, for 0.3 g/l of catalyst loading. The corresponding values when omitting

73

this law are about 0.82 and 1.51 W/m, respectively, which are not too far from those found by Raúl. Acosta et al. [31]. The OVRPA found by Ochoa-Gutierrez et al. [49] with 0.25 g/l of the catalyst loading was 15.12 W using the SFM-1D-HG and with the SFM-2D-HG, 16.35 W at the same operating conditions.

9. 1. 1. SFM-2D-HG in tubular and CPC photoreactors

The total amount of energy absorbed in a CPC is higher than in a tubular reactor since the CPC reactor receives radiation at its lower hemicylindrical wall thanks to its reflectors, which is not the case for a tubular reactor. Figure 14 shows that radiation absorption in CPC is more than 85 percent greater than in a tubular reactor using the SFM-2D-DR, and it is greater than that obtained by Colina-Márquez et al. [13] using the SFM-1D-DR. The method of discretization used in the mentioned studies [13, 31, 34] may be to blame for this disparity. Figure 15 represents the LVRPA profiles for a CPC (a) and a tubular reactor (b) at 0.5 g/l of catalyst loading with the HG phase function considering Lambert's cosine law.
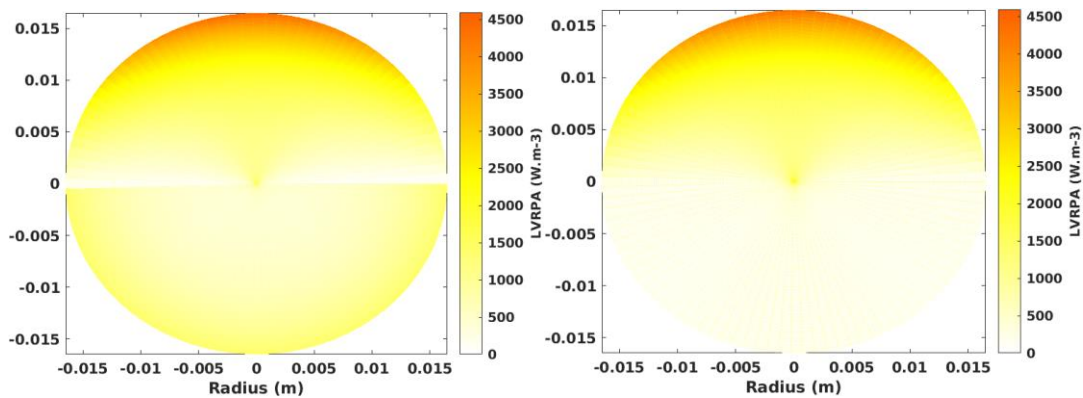
(a) SFM-HG-L-2D   (b) Tub-HG-L-2D

74
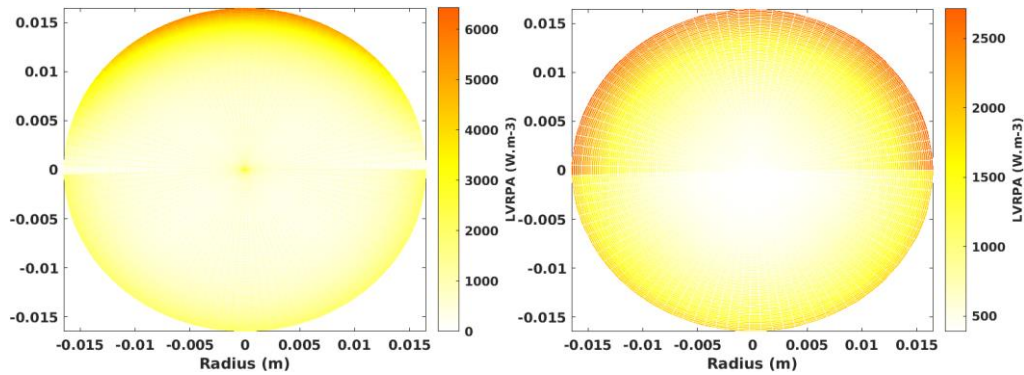
(c) SFM-DR-L-2D   (d) SFM-HG-2D

Fig. 15. LVRPA for a CPC and tubular reactors at 0.5 g/l of C_{cat}: a) CPC reactor with the HG phase function considering Lambert's cosine law, b) Tubular reactor with the HG phase function considering Lambert's cosine law, c) CPC reactor with the DR phase function considering Lambert's cosine law, and d) CPC reactor with the HG phase function without considering Lambert's cosine law.

9.1.2   Absorption behavior with the SFM-2D

The LVRPA profile (Figure 15) indicates a decrease in absorption from the reactor wall to its center, where absorption is essentially nil; these results are consistent with those previously reported [13, 31]. The decrease of the incident radiation at the reactor wall from the angle $\theta=\pi/2$ to the angle $\theta=0$ ($\theta=\pi$) is due to Lambert's cosine law effect. As the catalyst loading increases, the LVRPA profile shows that the absorption at the reactor wall increases exponentially, which is consistent with the

literature [50]. This is because the amount of exposed catalyst on the reactor surface and the back-scattering energy absorbed from the internal layer are both increasing. There is good uniformity in the energy absorption for catalyst loads less than 0.5g/l; above this value, the energy absorption uniformity diminishes greatly and the LVRPA increases significantly approaching the reactor wall due to the clouding effect. When the number of catalyst particles at the reactor wall increases, the absorption at the irradiated reactor surface saturates and inhibits photons from reaching the inner zones of the reactor [13].

9.1 3. Impact of the phase function on the radiation absorption

Diffuse reflectance (SFM-2D-DR) and Henyey-Greenstein phase functions (SFM-2D-HG) were utilized in this work to demonstrate the effect of phase function on photon absorption and scattering in tubular and CPC photoreactors in SFM-2D simulations. As reported in the literature [13,26], the scattering probabilities were evaluated using phase functions DR and HG. SFM-2D-DR and SFM-2D-HG photon absorption rates are shown in Figure 14 as a function of catalyst loading. To compare, the VRPA/H computed with the SFM-2D-DR is lower than that calculated with the SFM-2D-HG for both a CPC reactor and a tubular reactor operating at a catalyst loading of more than 2.1g/l. Due to its preference for forward scattering over backward scattering, the TiO_2-P25 catalyst particle yielded this result (the HG phase function asymmetric factor is about 0.53 for a titanium dioxide P25 [31]). Using the HG phase function, the absorption of photons in the inner reactor zone increases as a result of the deep penetration of photons. Another factor contributing to lower photon absorption in the reactor interior is the DR phase function preference for backward rather than forward scattering. Absorption at the reactor wall is higher with SFM-HG-2D than with SFM-DR-2D, as shown in Figures 15 (a) and (c). This behavior is because the backward scattering is higher with the SFM-DR-2D than with the SFM-HG-2D since, for the DR phase function, the backward scattering probability

is b = 0.71, which is more than six times greater than that for the HG phase function (b = 0.113) [31].

9.1. 4. SFM-HG-L-2D and SFM-HG-2D on CPC photoreactors

Fig. 14 indicates that, for any value of catalyst loading, the VRPA/H evaluated with the HG phase function and without Lambert's cosine law for a CPC (VRPA/H-CPC-HG green solid line) is around 50% higher than the VRPA/H calculated with the HG phase function and incorporating Lambert's cosine law for a CPC (VRPA/H-CPC-HG-L orange solid line). The same holds for the DR phase function as well. This behavior can be explained mathematically since, with Lambert's cosine law, the absorption of radiation is proportional to the cosine function, which varies between 0 and 1 [35]. There is an exponential increase in VRPA/H for catalyst loading up to 0.5 g/l approximately; over this value, the VRPA/H increases asymptotically toward a fixed value (Figure 14). The same behavior was observed by Brandi et al. [50] in a flat plate reactor and is different from that found by Colina-Márquez et al. [13], where the VRPA/H increased exponentially, reaching a peak, and then decreased asymptotically toward some constant value. This is due to the lower accuracy of the discretization used when adapting the SFM-1D to a CPC reactor [13]. These findings, however, do not negate the significance of the prior research [13, 31, 33, 37] cited in this paper. The slight increase in the VRPA/H over 0.5 g/l of catalyst loading is because of the clouding effect that prevents photons from diffusing into the inner regions of the reactor. Then, for catalyst loadings beyond 0.5 g/l, it would not be economically beneficial because of the waste of the catalyst. Therefore, for optimization purposes, a catalyst loading of between 0.1 and 0.5 g/l is recommended and not under 0.1 g/l since this means a low absorption of energy and subsequently less production of oxidizing species.
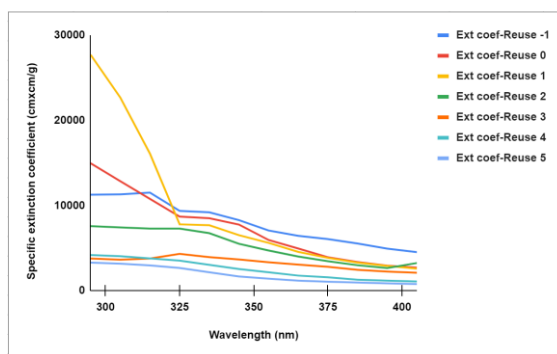
9.2   Evaluation of the LVRPA considering the catalyst reuse

The specific extinction, scattering, and absorption coefficients were determined for the fresh catalyst as well as for the used and reused catalyst using the procedure described in section 7.3 (see Fig. 16).
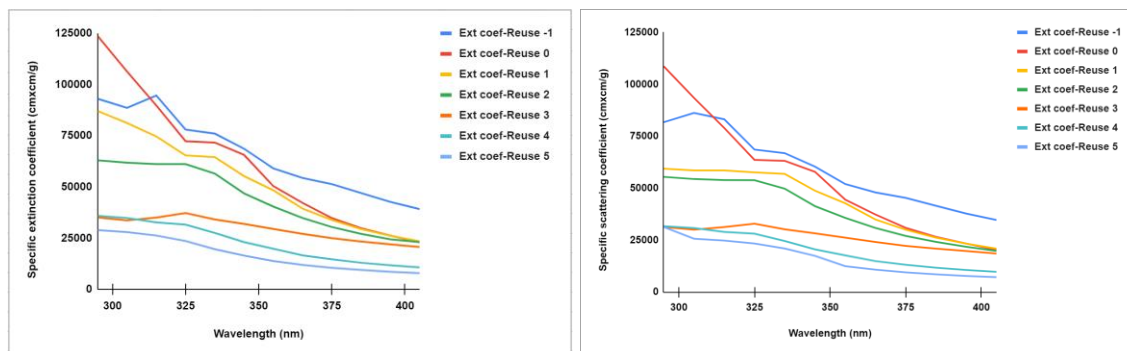
(a)

(b)

(c)

Fig. 16. Specific extinction (a), scattering (b), and absorption (c) coefficients (cm^2/g) vs wavelength (nm) for the fresh, used, and reused catalyst.

Figure 16 a) shows how the specific extinction coefficient varies as a function of the wavelength ([295; 405] nm). The specific extinction behavior and the results found in this figure for the fresh catalyst are in good agreement with those found in the literature (Cabrera et al., (1996); Satuf et al.,

(2006)). The same behavior was observed for each reused catalyst, and its extinction coefficient decreased each time it was reused. The average specific extinction coefficient and albedo found in this work (5072 m^2/kg, 0.88) were almost equal to that found by Satuf et al., (2005) (50901.73 m^2/kg, 0.86) and a little different from that found by H. Otálvaro et al., 2017 (57100 m^2/kg, 0.95). It is worth mentioning that Satuf et al. (2005) used a rigorous method while Otálvaro et al. (2017) used a simplified one. Table 4 shows the average optical properties of the catalyst for each reuse calculated in the wavelength interval [295; 405] nm (TiO$_2$ absorption UV spectrum) as follows:

$$\sigma = \frac{\int_{295}^{405} \sigma_\lambda I_\lambda d\lambda}{\int_{295}^{405} I_\lambda d\lambda} \tag{136}$$

$$\kappa = \frac{\int_{295}^{405} \kappa_\lambda I_\lambda d\lambda}{\int_{295}^{405} I_\lambda d\lambda} \tag{137}$$

Table 4. Average optical properties of the catalyst for each reuse.

N-Reuse	β^*(cm^2/g)	σ^*(cm^2/g)	κ^*(cm^2/g)	$\omega * 100$
N-Fresh	50719.42	44744.90	5974.52	88.27
0	37355.35	33010.29	4345.06	88.37
1	35438.60	31320.50	4118.10	88.38
2	32034.14	28180.56	3853.58	87.97
3	25090.61	22381.23	2709.38	89.2
4	15462.88	13847.14	1615.74	89.55
5	11181.57	10054.65	1126.92	89.92

For each catalyst, the LVRPA is essentially a function of the catalyst's optical properties, the catalyst loading, and the reactor geometry. The catalyst average optical properties were estimated and then introduced into the LVRPA, the VRPA/H, and the OVRPA. The specific extinction coefficient decreases as well as the specific absorption and scattering coefficients, whereas the albedo scattering increases when N-Reuse increases. N-Reuse represents the number of cycles of reuses here. N-Reuse = N-Fresh= -1 and N-Reuse = 0 represent the fresh and first-time catalysts, respectively. This implies that the VRPA decreases since it is proportional to the absorption coefficient. Figure 17. a), which depicts VRPA/H as a function of N-Reuse, confirmed the previous statement (catalyst loading of 0.3 g/L). The same behavior was observed when varying the catalyst loading (Figure 17. b)).

a)   b)
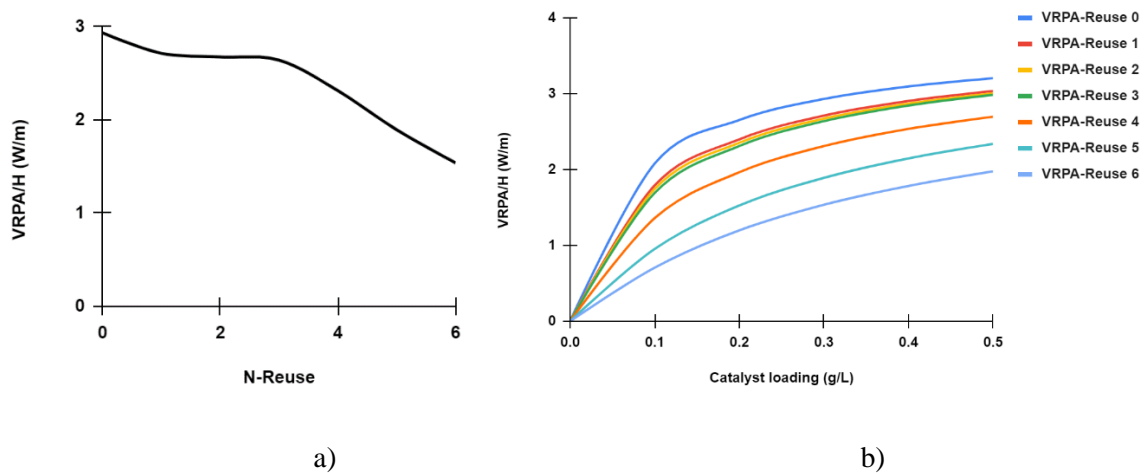
Fig. 17. VRPA/H behavior: a) VRPA/H behavior for 0.3 g/ L of TiO$_2$; b) VRPA/H vs Cat loading for each reuse.

Figure 18. a) shows the average catalyst optical properties variation in function of N-reuse. All those parameters decrease linearly with the increase of N-Reuse.
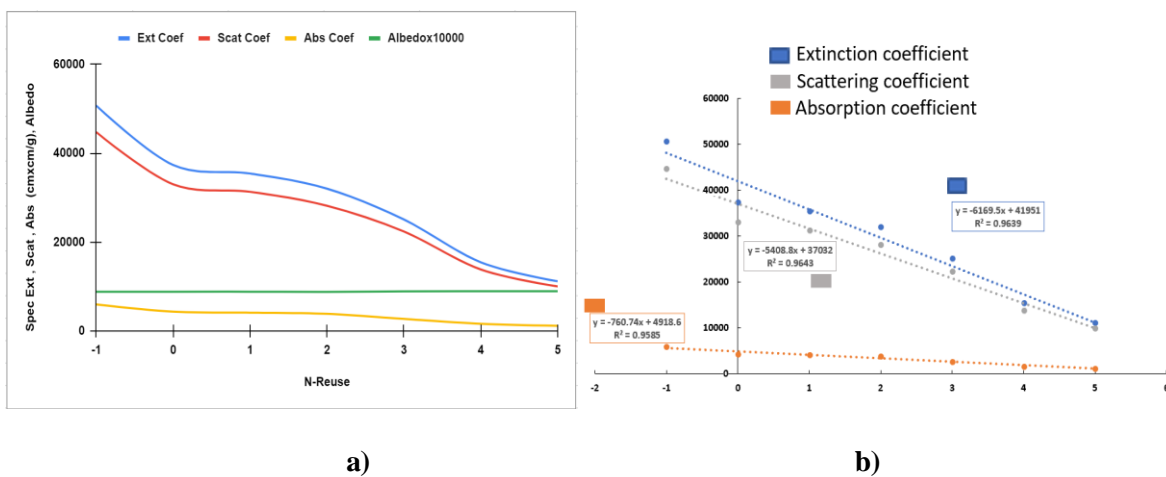
Fig. 18. a) Average optical properties of the catalyst for each reuse vs the order cycle of the catalyst reuse. b) Fitting of the catalyst average scattering, absorption, and extinction coefficients vs the order cycle of the catalyst reuse.

The fitting of the average optical properties of the catalyst (scattering, absorption, and extinction coefficients) with respect to the order of cycle of the catalyst reuse presented a linear behavior of each of these parameters with a correlation higher than 0.95 for each one (see Fig. 18. b)). The mathematical expressions of these parameters are expressed as follows:

$$\sigma_n = -5408.8n + 37032 \tag{138}$$

$$\kappa_n = -760.74n + 4918.6 \tag{139}$$

$$\beta_n = -6169.5n + 41951 \qquad\qquad (140)$$

where n represents N-Reuse which stands for the order of cycle of the catalyst reuse.

9.3. Kinetic model using the fresh catalyst

In section 9.1, during the simulation of the SFM-2D, it was found that the optimum catalyst loading (C_{cat}) that leads to the best photocatalytic efficiency is between 0.1 and 0.5 g/L at the solar scale. The apparent kinetic constants found for each of the five experiments carried out with the fresh catalyst (0.1; 0.2; 0.3; 0.4; 0.5 g/L) are listed in Table 5, and 0.3 g/L was found to be the optimum catalyst loading. This value is not far from that found in the literature [13].

Table 5. Kinetic parameters for each experiment with the fresh catalyst.

C_{cat} (g/L)	0.1	0.2	0.3	0.4	0.5
k_{app} (min^{-1})	0.112	0.253	0.281	0.122	0.267
k_p ($W^{-0.5}m^{1.5}min$)	3.8 x10^{-3}	7 x10^{-3}	8 x10^{-3}	3.38 x10^{-3}	7.27 x10^{-3}

k_{app} was found by plotting $\ln\left(\frac{C}{C_0}\right)$ versus time (t_{30w}) using experimental data of the degradation with a correlation greater than 0.9 for each experiment. Figure 19 shows a satisfactory fit of the

concentration curves by the model presented in this work for the five experiments. The rate of degradation was faster for the catalyst loading of 0.3 g/L and lower for 0.1 g/L, probably because the generation of hydroxyl radicals reached its maximum at 0.3 g/L and for 0.1 g/L there was less production of hydroxyl radicals.
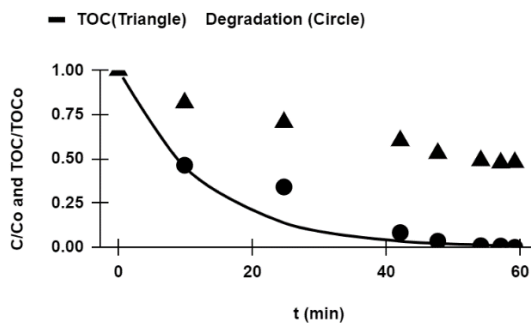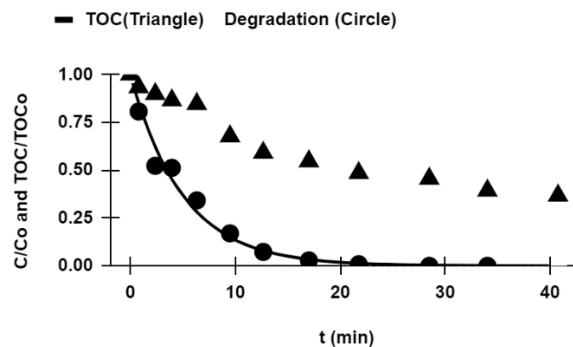

a)
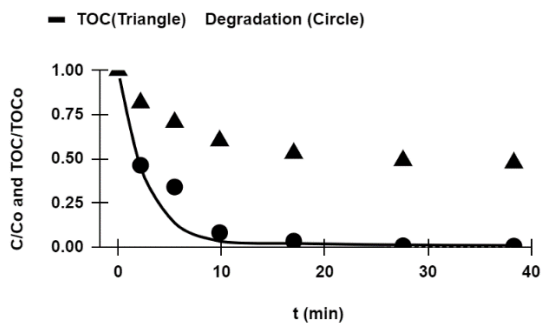
b)
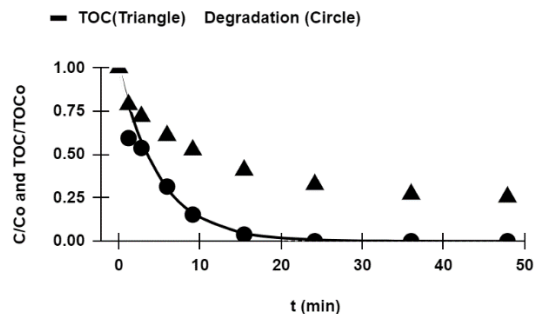
c)
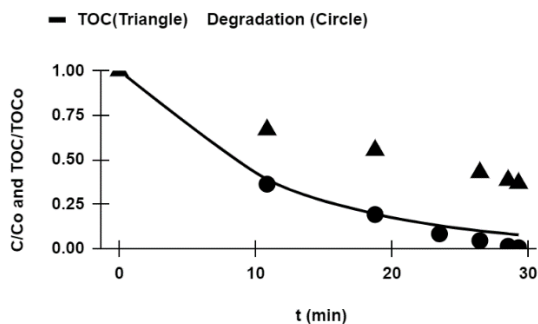
d)

e)

Fig. 19. Normalized degradation and mineralization vs time (t_{30w}), a)Catalyst loading 0.1 g/ L, b) Catalyst loading 0.2 g/ L, c) Catalyst loading 0.3 g/ L, d) Catalyst loading 0.4 g/ L, e) Catalyst loading 0.5 g/ L.

The five experiments reached complete degradation and more than 54 % of TOC removal in less than 40 minutes, except for 0.1 g/L of the catalyst loading. The concentration of 0.3g/L was also the optimum catalyst loading that reached the best mineralization percentage (67 % in 24.14 min). Tables 6 and 7 show the percentage of degradation and mineralization with the corresponding time for each experiment. The model was fitted by using as a reference 0.3 g/L of catalyst loading and then varying the initial concentration of the catalyst (0.1, 0.2, 0.4, and 0.5 g/L) (see Fig. 20). The discrepancies with 0.2 and 0.5 g/L were almost negligible and higher with 0.1 and 0.4 g/L. The higher discrepancies found with 0.1 and 0.4 g/L could be attributed to the low amount of catalyst loading and experimental errors during the process, respectively. The chromatograph of the degradation of the SMX at 0.3 g/L of catalyst loading is shown in Figure 1 of the annex section.
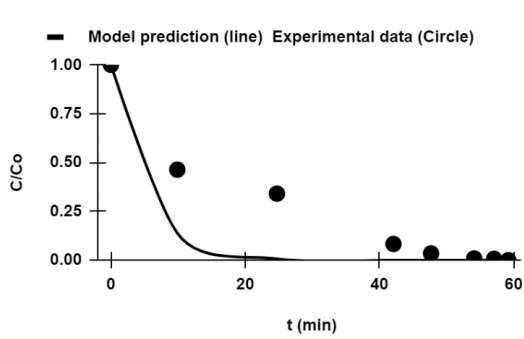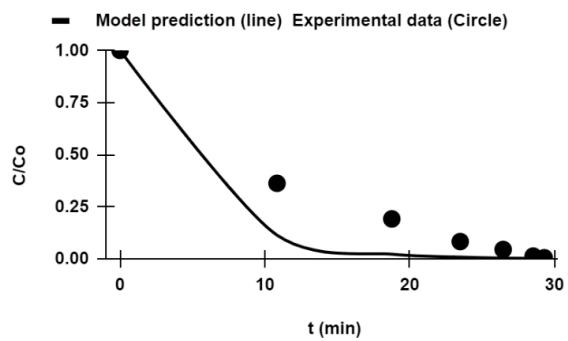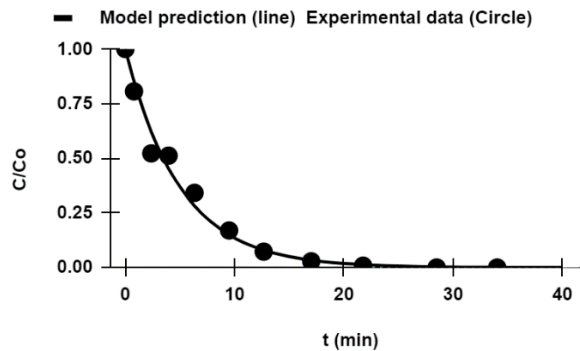
a)
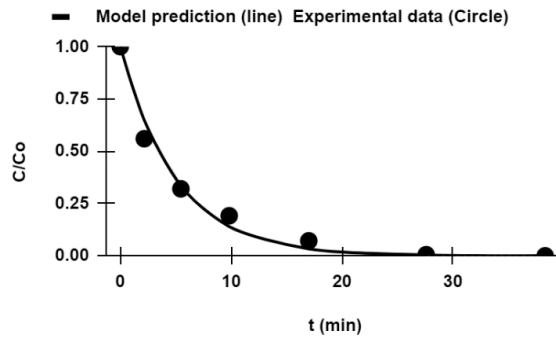
b)
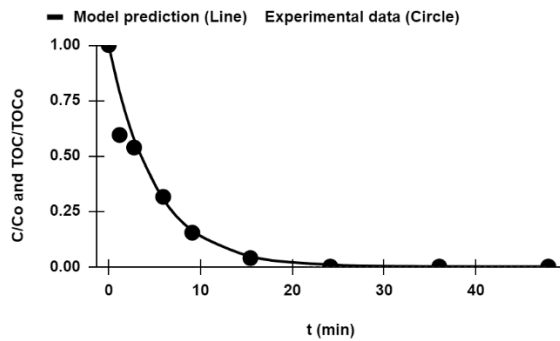
c)

d)

e)

Fig. 20. Kinetic model fitting (fresh catalyst) with catalyst loading: a) 0.1 g/ L, b) 0.2 g/ L,

b) 0.3 g/ L, d) 0.4 g/ L and e) 0.5 g/ L.

Table 6. Maximum percentage of SMX degradation and mineralization for each experiment (fresh catalyst).

C_{cat} (g/L)	0.1	0.2	0.3	0.4	0.5
t_{30W} (min)	59.21	38.33	24.14	30	28.5
% Degradation	100	100	100	100	100
% Mineralization	47.67	64	67	53.37	55

Table 7. Percentage of SMX degradation and mineralization for each experiment for about 10 minutes (fresh catalyst)**.**

C_{cat} (g/L)	0.1	0.2	0.3	0.4	0.5
t_{30W} (min)	9.89	9.83	9.10	10.84	9.5
% Degradation	53.25	80.87	84.7	63.7	83
% Mineralization	18.37	36.84	47.45	33.17	32

With 0.3 g/L of catalyst loading, the TOC removal increased up to 71 % after 48 minutes (see Figure

19 c)); this proves that by increasing the experimental time, the TOC removal also increased and probably could reach 100 %. Usually, SMX mineralization is slower than its degradation [51].
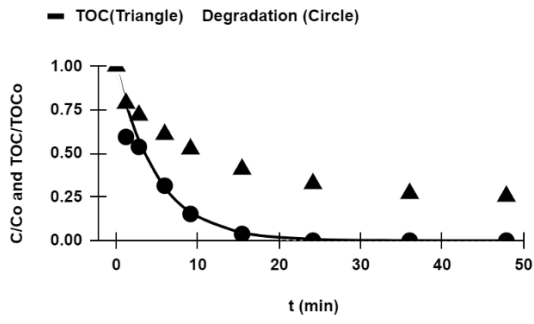
9.4. Kinetic model considering the catalyst reuse

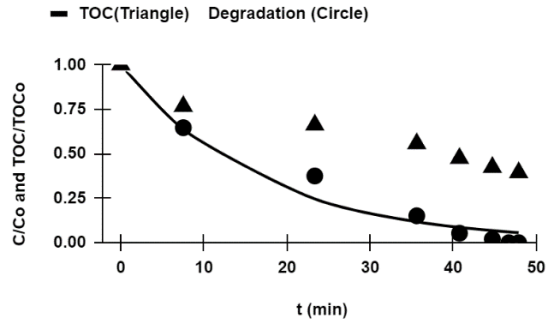**Table 8.** Percentage of SMX degradation and mineralization for each cycle of catalyst reuse.

N-Reuse	0	1	2	3	4	5
t_{30w} (min)	24.14	46.7	67.28	75.2	90	115
% Degradation	100	100	100	100	100	100
% Mineralization	67	60	44	60	51	56

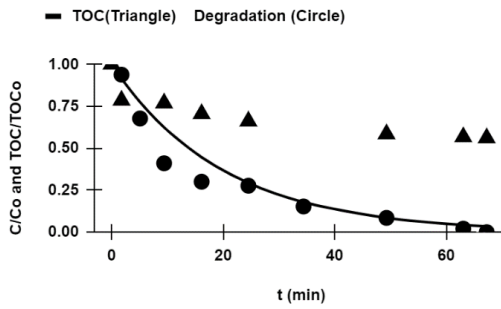**Table 9.** Percentage of SMX degradation and mineralization for each cycle of catalyst reuse after about 50 minutes.

N-Reuse	0	1	2	3	4	5
t_{30w} (min)	47.88	47.88	49.31	49.47	50.57	48.08
% Degradation	100	100	93	94	85	65
% Mineralization	71	60	44	56.4	33	37

TOC(Triangle)   Degradation (Circle)

a)

TOC(Triangle)   Degradation (Circle)

b)

TOC(Triangle)   Degradation (Circle)

c)

TOC(Triangle)   Degradation (Circle)

d)

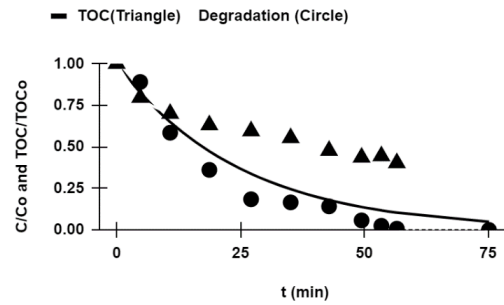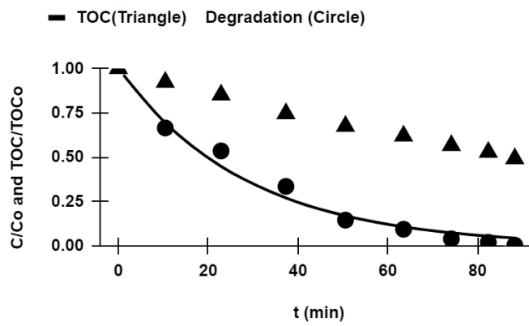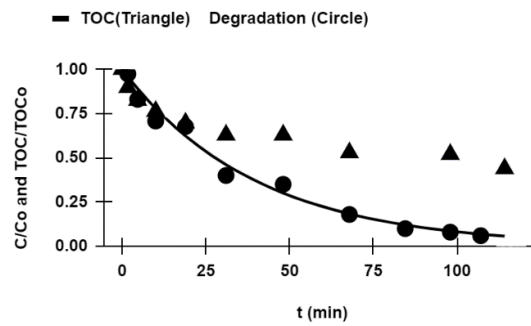TOC(Triangle)   Degradation (Circle)

e)

TOC(Triangle)   Degradation (Circle)

f)

Fig. 21. Normalized degradation and mineralization vs time (t_{30w}) (Catalyst reuse),

a) 1st use, b) 1st reuse, c) 2nd reuse, d) 3rd reuse, e) 4th reuse, f) 5th reuse.

Table 10. Kinetic parameters for each cycle of reuse.

N-Reuse	0	1	2	3	4	5
$k_{app,n}$ (min^{-1})	0.281	0.0843	0.0702	0.0562	0.0421	0.0351
$k_{p,n}$(W$^{-0.5}$m$^{1.5}$min)	8 x10^{-3}	2.5 x10^{-3}	2.09 x10^{-3}	1.69 x10^{-3}	1.35 x10^{-3}	1.24 x10^{-3}

Table 11. VRPA/H for each cycle of reuse and varying the catalyst loading.

C_{cat} (g/L)	0.1	0.2	0.3	0.4	0.5
(VRPA/H)$_0$	1.67	1.94	2.02	2.07	2.1
(VRPA/H)$_1$	1.47	1.85	1.96	2.01	2.05
(VRPA/H)$_2$	1.44	1.83	1.92	2.00	2.04
(VRPA/H)$_3$	1.39	1.81	1.84	1.98	2.02
(VRPA/H)$_4$	1.08	1.6	1.78	1.86	1.91
(VRPA/H)$_5$	0.66	1.24	1.54	1.69	1.78
(VRPA/H)$_6$	0.43	0.94	1.28	1.49	1.62

For the formulation of the kinetic model considering the catalyst reuse, a relationship was established

between the apparent kinetic constant for the nth reuse $k_{app,n}$ and for the initial use

$k_{app,0}$ as follows:

$$k_{app,n} = -\frac{v_T}{v_R}a_1(n-1) + a_2 k_{app,0}, n > 0 \tag{141}$$

where $a_1 = 2.56 \times 10^{-4}$ and $a_2 = 0.3$ are dimensionless constants.

$$k_{app,0} = k_{p,0}\sqrt{\frac{OVRPA_0}{v_R}}, k_{p,0} = k_0 K_0 \tag{142}$$

$$k_{app,n} = k_{p,n}\sqrt{\frac{OVRPA_n}{v_R}}, k_{p,n} = k_n K_n \tag{143}$$

where $OVRPA_0$ and $OVRPA_n$ $n > 0$ are the OVRPA for the first use and n^{th} reuse of the catalyst, respectively. Table 11 shows the value of $OVRPA_n$ for n from 0 to 6 and for catalyst loading of 0.1, 0.2, 0.3, 0.4, and 0.5 g/ L.
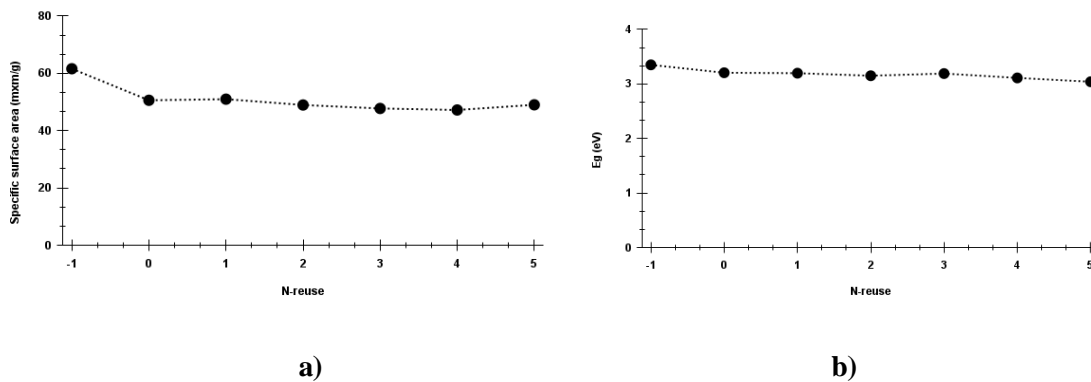
Then, the kinetic equation for the nth reuse will be defined as:

$$C_n = C_0 e^{-\frac{v_R}{v_T}k_{app,n}t_{30W}} \tag{144}$$

The model fit the first four reuses perfectly because the apparent kinetic constants coincided with those found in Table 10, but there was a 6% discrepancy with the fifth reuse (see Figure 22).
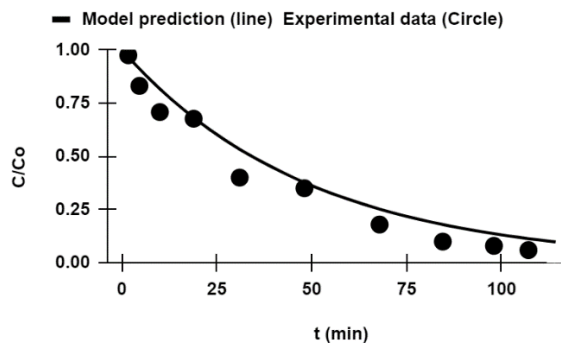
Fig. 22. Fitting of the kinetic model with the data of the 5th cycle of reuse.

a)	b)

Fig. 23. a) Specific surface area vs N-Reuse, b) Bandgap vs N-Reuse.

The catalyst band gap (Eg) was analyzed by spectroscopy of diffuse UV-Vis reflectance (DRS) (see Figure 2 Annex section). The determination of the catalyst specific surface area was performed from the nitrogen adsorption-desorption isotherms using the Brunauer–Emmett–Teller (BET) method (see Figure 3 Annex section).

Figure 23 shows the variation of the specific surface area (Figure 23 a)) and the bandgap (Figure 23 b)) as a function of N-Reuse. The specific surface area decreased by up to 18% after the first catalyst use (see Figure 23 a). This could probably justify the fact that the apparent kinetic constant of the degradation using the fresh catalyst is much greater than that of the first cycle of reuse (see Table 10). Then, after the first catalyst use, the variation of the specific surface area is depreciable (less than 2% of the initial specific surface area). It increased and decreased from the first until the fifth cycle of the catalyst reuse. This means there was adsorption onto and desorption from the catalyst surface from one cycle to another, and the depletion of the SMX degradation could also come from the fact that the catalyst has lost its absorptivity. For each cycle of reuse, the specific surface area of the catalyst and its bandgap were measured, and both were found to decrease (see Figure 23). Figure 23 could be explained by the fact that the intermediates produced by the SMX degradation were adsorbed on the catalyst surface, occupying active sites and acting as sensitizers but impeding new SMX molecules from being adsorbed. This probably favored the recombination process of e^-/h^+ pairs and could explain why the SMX degradation decreased cycle after cycle. SMX is known as a molecule that absorbs light between 240 and 310 nm [51]. This means there is no significant competition between the SMX molecules and the catalyst particles in light absorption. A different scenario could be observed with SMX byproducts, which could compete with TiO_2 particles. If that was the case, light could not easily get onto the catalyst surface and no oxidizing species could be generated. All this could justify the depletion of the SMX degradation, but an extra study should be conducted to get more information about that.

9.5 Model predictions

It would be interesting to know how long the photocatalysis process would keep being active. It is

necessary to solve Eq. (145) since that means no variation of the substrate concentration during the experimental time.

$$C_n = C_0 e^{-\frac{v_R}{v_T}k_{app,n}t_{30W}} = C_0 \tag{145}$$

Eq. (145) is equivalent to,

$$k_{app,n} = -\frac{v_T}{v_R}a_1(n-1) + a_2 k_{app,0} = 0 \tag{146}$$

which implies,

$$n = \frac{a_2}{a_1}\frac{v_R}{v_T}k_{app,0} + 1 = 7 \tag{146}$$

Therefore, with the model predictions, after seven cycles of reuse, approximately, the catalyst would no longer significantly absorb the incident solar energy supplied to the system. Consequently, only the photolysis process would be mainly active. Figure 24 shows the model predictions for the 6th and 7th cycles of the catalyst reuse during 300 minutes of experimental time.
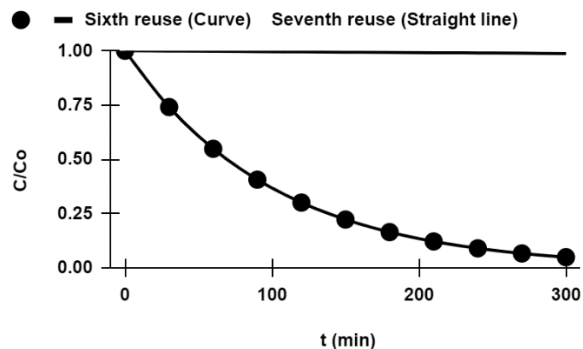
Fig. 24. Model predictions for the 6th and 7th cycles of the catalyst reuse.

10 Our investigation, green chemistry, and sustainability

Sustainability and green chemistry essentially go hand in hand. Sustainability contributes to meeting the needs of the present generation without compromising the ability of future generations to meet their needs. It has three main components: economic, environmental, and social. On the other hand, the US Environmental Protection Agency (EPA) defined "green (sustainable) chemistry" as the use of chemistry for pollution prevention and the design of chemical products and processes that are more environmentally benign (Gabriele Centi and Siglinda Perathoner, 2003). It is one of the most fundamental and powerful tools to use on the path of sustainability (Suresh D. Dhage and Komalsing K. Shisodiya, 2013). It embodies twelve principles, and this work covers at least three of them. For instance, catalysis (catalysis is the ninth principle). In chemistry, catalysis is the cleavage of chemical bonds in the presence of a substance (a catalyst) that accelerates the rate of a chemical reaction without being consumed. Thus, using a catalyst reduces the time and energy of a chemical reaction. The catalyst used in this work (TiO_2-P25) is less toxic, cheaper, and abundant in nature. Hence, using TiO_2-P25 improves the second principle of green chemistry (atom economy). The seventh principle of green chemistry was applied since sunlight (renewable energy) was used as the radiant source. All

the experiments carried out in this work led to complete degradation and more than fifty percent of mineralization. It was found that the TOC removal could be increased by extending the experimental time. Then, water obtained after the photocatalytic experiments could be reused or discharged into our environment without harming living organisms. A mathematical model formulated could help with predictions, optimization, and cost limitation. The catalyst reusability also proves the sustainability of this project. Nevertheless, this project is not perfectly sustainable since an electrical source was used to power up the CPC reactor, but this could be improved by using solar panels.

11 Conclusions

Based on a two-dimensional SFM, a new model was developed to estimate the radiative field in a solar CPC photoreactor. A simple analytical equation was developed for tubular photoreactors using Lambert's cosine law as a suitable boundary condition. In light of Lambert's cosine law, the SFM results were shown to be more in line with the RTE than when it was excluded. The calculated VRPA/H and OVRPA values agreed with those found in previous investigations. These two parameters are the most commonly employed when it comes to photoreactors used in water treatment. The experiment with 0.3 g/L of catalyst loading was the fastest to reach complete degradation and had the highest mineralization percentage. For each cycle of the catalyst reuse carried out, the specific surface area of the catalyst and its bandgap were measured. Both were found to decrease, as well as the specific absorption and scattering coefficients. The OVRPA was evaluated and was found to decrease from the first to the fifth cycle. This could also explain the SMX degradation depletion from the first to the fifth cycle. A kinetic model containing a similar mathematical structure as the L-H kinetic model combined with the radiant field was used to describe the photocatalytic degradation of SMX considering the catalyst reuse. This model was formulated with the experimental data of the

four first cycles of the catalyst reuse and was validated with the 5th cycle with a discrepancy of 6 %. Predictions from the model stipulated that the catalyst would become useless after the 7th cycle of reuse.

12 Perspectives

Future work with SFM-2D will examine the model's applicability and extension to various geometries, simulation, and comparison with other approaches like P1, MC, and RTE-DOM-CFD. Furthermore, accurately predicting a phase function is capable of characterizing the behavior of any catalyst. The extension of the six scattering directions to N scattering directions with N>6 and the derivation of an analytical expression for the radiation flux distribution on the lower side of the CPC wall. Then, the formulation of a kinetic model taking into account hydrodynamic, mass transfer, diffusional, and temperature effects on heterogeneous photocatalysis. Finally, to investigate catalyst reuse in the context of other types of catalysts other than commercial titanium dioxide TiO_2-P25.

13 References

[1] B. Cattaneo, Emerging pollutants, https://ec.europa.eu/jrc/ en/news/emerging-pollutants-growing-concern-our-oceans, accessed 11 November 2020.

[2] O'Flynn, D., Lawler, J., Yusuf, A., Parle-McDermott, A., Harold, D., Mc Cloughlin, T., … White, B. A review of pharmaceutical occurrence and pathways in the aquatic environment in the context of a changing climate and the COVID-19 pandemic. Analytical Methods, 2021, 13(5), 575–594. doi:10.1039/d0ay02098b

[3] H. Leckie, R. Lacy, B. Diderich and X. Leaive, Pharmaceutical residues in freshwater: hazards

and policy responses, OECD Publishing, Paris, 2019.

[4] A. J. Ebele, M. Abou-Elwafa Abdallah and S. Harrad, Pharmaceuticals and personal care products (PPCPs) in the freshwater aquatic environment, Emerging Contaminants, 2017, 3, 1–16.

[5] Kanakaraju, D., Glass, B. D., & Oelgemöller, M. Titanium dioxide photocatalysis for pharmaceutical wastewater treatment. Environmental Chemistry Letters, 2013, 12(1), 27–47. doi:10.1007/s10311-013-0428-0

[6] Parrino, F., Loddo, V., Augugliaro, V., Camera-Roda, G., Palmisano, G., Palmisano, L., & Yurdakal, S. Heterogeneous photocatalysis: guidelines on experimental setup, catalyst characterization, interpretation, and assessment of reactivity. Catalysis Reviews, 2018, 1–51. doi:10.1080/01614940.2018.1546445

[7] Juan Carlos Colmenares and Rafael Luque '' Heterogeneous photocatalytic nanomaterials: prospects and challenges in selective transformations of biomass-derived compounds'' DOI: 10.1039/C3CS60262A (Tutorial Review) Chem. Soc. Rev., 2014, 43, 765-778

[8] Ternes, T.; Joss, A. Human Pharmaceuticals, Hormones and Fragrances. The Challenge of Micropollutants in Urban Water Management; IWA Publishing: London, UK, 2006.

[9] Xekoukoulotakis, N. P., Drosou, C., Brebou, C., Chatzisymeon, E., Hapeshi, E., Fatta-Kassinos, D., & Mantzavinos, D. Kinetics of UV-A/TiO_2 photocatalytic degradation and mineralization of the antibiotic sulfamethoxazole in aqueous matrices. Catalysis Today, 2011, 161(1), 163–168. doi:10.1016/j.cattod.2010.09.027

[10] Diego Alejandro Pino-Sandoval · Laura Hinojosa-Reyes · Jorge Luis Guzmán-Mar · Juan Camilo Murillo-Sierra · Aracely Hernández-Ramírez. Solar Photocatalysis for Degradation of Pharmaceuticals in Hospital Wastewater: Influence of the Type of Catalyst, Aqueous Matrix, and Toxicity Evaluation, Water Air Pollut 233: (2022) 14. https://doi.org/10.1007/s11270-021-05484-7

[11] Hoffmann, M. R.; Martin, S. T.; Choi, W.; Bahnemann, D. W. Environmental applications of semiconductor photocatalysis. Chem. Rev. 1995, 95, 69–96. https://doi.org/10.1021/cr00033a004

[12] Fujishima, A.; Rao, T. N.; Trek, D. A. Titanium dioxide photocatalysis. J. Photochem. Photobiol.

C: Photochem. Rev. 2000, 1, 1–21. https://doi.org/10.1016/S1389-5567(00)00002-2

[13] José Colina-Márquez, Fiderman, Machuca-Martinez, Gianluca Li Puma Radiation absorption and optimization of solar photocatalytic reactors for environmental applications. (Environ. Sci.Technol.2010, 44, 5112-5120). https://doi.org/10.1021/es100130h

[14] José Colina-Márquez, Fiderman, Machuca-Martinez, Gianluca Li Puma Photocatalytic Mineralization of Commercial Herbicides in a Pilot-Scale Solar CPC Reactor: Photoreactor Modeling and Reaction Kinetics Constants Independent of Radiation Field. (Environ. Sci.Technol.2010, 44, 5112-5120). https://doi.org/10.1021/es902004b

[15] A. Cassano, O. Alfano. "Reaction engineering of suspended solid heterogeneous photocatalytic reactors". Catalysis Today, (2000) vol. 58, pp.167-197. https://doi.org/10.1016/S0920-5861(00)00251-0

[16] M. Satuf, R. Brandi, O. Alfano, A. Cassano. "Modeling of a Flat Plate, Slurry Reactor for the Photocatalytic Degradation of 4-Chlorophenol". International Journal of Chemical Reactor Engineering, (2007) vol. 5, no. A59. https://doi.org/10.2202/1542-6580.1539

[17] R. Siegel, J. Howell, Thermal Radiation Heat Transfer, Third, Hemisphere Publishing Corporation, Washington. DC, 1992.

[18] Kourganoff, V., "Basic Methods in Transfer Problems." London, Oxford Press, 1952. Journal Pre-proof

[19] PvIark, J, C., "The Spherical Harmonic Method, I and 11." National Research Council of Canada. CRT-340 and CRT-338 Oune, 1957.

[20] Spencer, V., and Fano, U., "Penetration and Diffusion of X-rays." Physical Review, Vol. 88, (1952), p. 793. X-Rays, Calculation of Spatial Distributions by Semi Asymptotic Methods." Physical Review, Vol. 88, (1952), p. 793. https://doi.org/10.1103/PhysRev.88.793

[21] Zhen-Juan Li, Xiao-Lei Li, Xin-Lin Xia & Chuang Sun. A hybrid strategy for solving radiation-conduction in irregular geometries filled with gray semitransparent medium using Monte Carlo method combined with blocked-off and embedded boundary treatments. Numerical Heat Transfer,

Part B: Fundamentals, 1-20 (2019). https://doi.org/10.1080/10407790.2019.1690368.

[22] M.A. Ramírez-Cabrera, P.J. Valadés-Pelayo, C.A. Arancibia-Bulnes, E. Ramos, Validity of the Six-Flux model for photoreactors, Chem. Eng. J. 330 (2017) 272–280. doi: http://dx.doi.org/10.1016/j.cej. 2017.07.120

[23] Theissing, H. H., "Macrodistribution of Light Scattering by Dispersions of Spherical Dielectric Particles''. Journal of the Optical Society, Vol. 40 (1950), p. 232. https://doi.org/10.1364/JOSA.40.000232

[24] Fritz, S., "Scattering and Absorption of Solar Energy by Clouds," Ph.D. Thesis, Massachusetts Institute of Technology (1953).

[25] Chu, C. Xi., and Churchill, S. W., Numerical Solution of (1953). Problems in Multiple Scattering of Electromagnetic Radiation. Journal of Physical Chemistry, 1701. 59 (1955), p. 855. https://doi.org/10.1021/j150531a013

[26] A. Brucato, A. Cassano, F. Grisafi, G. Montante, L. Rizzuti, G. Vella. "Estimating radiant fields in flat heterogeneous photoreactors by the six-flux model". American Institute of Chemical Engineers, (2006) vol. 52, no.11, pp.3882-3890. https://doi.org/10.1002/aic.10984

[27] C. Chu, S. Churchill. "Multiple scattering by randomly distributed obstacles: Methods of solution". Antennas and Propagation, (1956) vol. 4, no.2, pp.142-148. https://doi.10. 1109/tap.1956.1144373 Journal Pre-proof

[28] W. Houf, F. Incropera. "An assessment of techniques for predicting radiation transfer in aqueous media". Journal of Quantitative Spectroscopy and Radiative Transfer, (1980) vol. 23, pp.101-115. https://doi.org/10.1016/S0022-4073(80)80009-4

[29] R. Koenigsdorff, F. Miller, R. Ziegler. "Calculation of scattering fractions for use in radiative flux models". International Journal of Heat and Mass Transfer, (1991) vol. 34, pp.2673-2676. https://doi:10.1016/0017-9310(91)90107

[30] G. Li Puma, J. Nee Kohr, A. Brucato. "Modeling of an annular photocatalytic reactor of water purification: Oxidation of pesticides". Environmental Science Technology, (2004) vol. 38, pp.3737-

3745. https://doi.10.1021/es0301020

[31] Raul Acosta-Herazo, Jesus Monterroza-Romero, Miguel Angel Mueses, Fiderman MachucaMartinez, Gianluca Li Puma "Coupling the Six-Flux absorption-scattering model to the HenyeyGreenstein scattering phase function: Evaluation and optimization of radiation absorption in solar photoreactors" Journal Contribution posted on 18.08.2016,03:57. https://doi.org/10.1016/j.cej.2016.04.127

[32] Li Puma, A. Gora, B. Toepfer. "Photocatalytic oxidation of multicomponent solutions of herbicides: Reaction kinetics analysis with explicit photon absorption effects". Applied Catalysis B: Environmental, (2006) vol. 68, pp.171-180. https://doi.org/10.1016/j.apcatb.2006.06.020

[33] M.A. Mueses, F. Machuca-Martínez, A. Hernández-Ramirez, G. Li Puma, Effective radiation field model to scattering- absorption applied in heterogeneous photocatalytic reactors, Chen. Eng. J. 279 (2015) 442-451. https://doi.org/10.1016/j.cej.2015.05.056

[34] Raúl Acosta-Herazo, Briyith Cañaveral-Velásquez, Katrin Pérez-Giraldo, Miguel A. Mueses, María H. Pinzón-Cárdenas and Fiderman Machuca-Martínez. A MATLAB-Based Application for Modeling and Simulation of Solar Slurry Photocatalytic Reactors for Environmental Applications. Water, 12(18), 2196. (2020). Doi: 10.3390/W12082196

[35] Reifsnyder, W. E. Radiation geometry in the measurement and interpretation of radiation balance. Agricultural Meteorology, 4(4), (1967), 255–265. https://doi.org/10.1016/0002-1571(67)90026-X

[36] Otálvaro-Marín, H. L., Mueses, M. A., Crittenden, J. C., & Machuca-Martinez, F. Solar photoreactor design by the photon path length and optimization of the radiant field in a TiO_2 - Journal Pre-proof based CPC reactor. Chemical Engineering Journal, 315, 283–295, (2017). doi:10.1016/j.cej.2017.01.019

[37] H.L. Otálvaro-Marín, F. González-Caicedo, A. Arce-Sarria, M.A. Mueses, J.C. Crittenden, F. Machuca-Martinez, Scaling-up a heterogeneous H_2O_2/TiO_2/solar- radiation system using the Damköhler number, Chem. Eng. J. 364 (2019) 244–256. doi:10.1016/j.cej.2019.01.141

[38] Jennyfer Diaz-Angulo, Jose Lara-Ramos, Miguel Mueses, Aracely Hernández-Ramírez, Gianluca Li Puma, Fiderman Machuca-Martínez, Enhancement of the oxidative removal of diclofenac and of the TiO$_2$ rate of photon absorption in dye-sensitized solar pilot scale CPC photocatalytic reactors, Chemical Engineering Journal (2019) 122520. doi: 10.1016/j.cej.2019.122520

[39] Miguel Angel Mueses, José Colina-Márquez, Fiderman Machuca-Martínez and Gianluca Li Puma. Recent advances on modeling of solar heterogeneous photocatalytic reactors applied for degradation of pharmaceuticals and emerging organic contaminants in water. Current Opinion in Green and Sustainable Chemistry (2021), 30:100486. doi.org/10.1016/j.cogsc.2021.100486

[40] Moreira, R. P. M., & Puma, G. L. Multiphysics Computational Fluid-Dynamics (CFD) Modeling of Annular Photocatalytic Reactors by the Discrete ordinates Method (DOM) and the Six-Flux Model (SFM) and Evaluation of the Contaminant Intrinsic Kinetics Constants. Catalyst Today (2020). https://doi.org/10.1016/j.cattod.2020.01.012

[41] Núñez-Salas, R. E., Hernández-Ramírez, A., Santos-Lozano, V., Hinojosa-Reyes, L., Guzmán-Mar, J. L., Gracia-Pinilla, M. Á., & Maya-Treviño, M. de L. Synthesis, characterization, and photocatalytic performance of FeTiO3/ZnO on ciprofloxacin degradation. Journal of Photochemistry and Photobiology A: Chemistry, 411, (2021), 113186. doi:10.1016/j.jphotochem.2021.113

[42] Gar Alalm, M., Samy, M., Ookawara, S., & Ohno, T. Immobilization of S-TiO$_2$ on reusable aluminum plates by polysiloxane for photocatalytic degradation of 2,4-dichlorophenol in water. Journal of Water Process Engineering, 26, (2018), 329–335. doi:10.1016/j.jwpe.2018.11.001

[43] Minh Tri, N. L., Kim, J., Giang, B. L., Al Tahtamouni, T. M., Huong, P. T., Lee, C., … Quang Trung, D. Ag-doped graphitic carbon nitride photocatalyst with remarkably enhanced photocatalytic activity towards antibiotic in hospital wastewater under solar light. Journal of Industrial and Engineering Chemistry. (2019). doi:10.1016/j.jiec.2019.08.037

[44] Arancibia-Bulnes, C. A., Jiménez, A. E., & Estrada, C. A. Development and Modeling of Solar Photocatalytic Reactor. Advances in Chemical Engineering, (2009) 185-227.

https://doi.org/10.1016/S0065-2377(09)00406-2

[45] Borowska, E., Gomes, J. F., Martins, R. C., Quinta-Ferreira, R. M., Horn, H., & Gmurek, M. Solar Photocatalytic Degradation of Sulfamethoxazole by TiO2 Modified with Noble Metals. Catalysts, 9(6), 500, 2019. doi:10.3390/catal9060500

[46] Montero-Ocampo, C., Gago, A., Abadias, G., Gombert, B., & Alonso-Vante, N. In situ photoelectrochemical/photocatalytic study of a dye discoloration in a microreactor system using TiO2 thin films. Environmental Science and Pollution Research, 19(9), 2012, 3751–3762. doi:10.1007/s11356-012-0771-x

[47] Malato, S.; Blanco, J.; Fernandez-Alba, A. R.; Aguera, A. Solar photocatalytic mineralization of commercial pesticides: Acrinathrin. Chemosphere 2000, 40, 403–40. https://doi.org/10.1016/S0045-6535(99)00267-2

[48] Malato, S.; Blanco, J.; Vidal, A.; Fernández, P.; Cáceres, J.; Trincado, P.; Oliveira, J. C.; Vincent, M. New large solar photocatalytic plant: set-up and preliminary results. Chemosphere 2002, 47, 235–240. https://doi.org/10.1016/S0045-6535(01)00220-X

[49] Ochoa-Gutiérrez, K. S., Tabarez-Aguilar, E., Mueses, M. Á., Machuca-Martínez, F., & Li Puma, G. A Novel Prototype Offset Multi Tubular Photoreactor (OMTP) for Solar Photocatalytic Degradation of Water Contaminants. Chemical Engineering Journal, 341, 628-638. (2018). https://doi.org/10.1016/j.cej.2018.02.068

[50] R. J. Brandi, O. M. Alfano, and A. E. Cassano, "Modeling of radiation absorption in a flat plate photocatalytic reactor," Chemical Engineering Science, vol. 51, no. 11, pp. 3169–3174, 1996. https://doi.org/10.1016/0009-2509(96)002

[51] Abellán, M. N., Giménez, J., & Esplugas, S. Photocatalytic degradation of antibiotics: The case of sulfamethoxazole and trimethoprim. Catalysis Today, 144(1-2), 131–136, (2009). doi:10.1016/j.cattod.2009.01.051
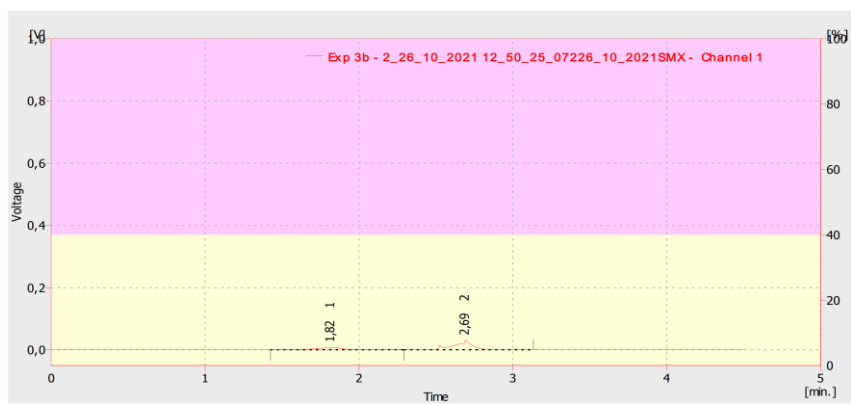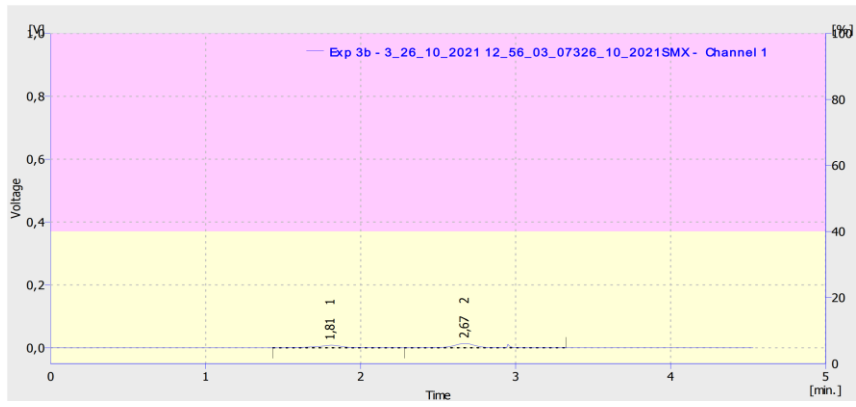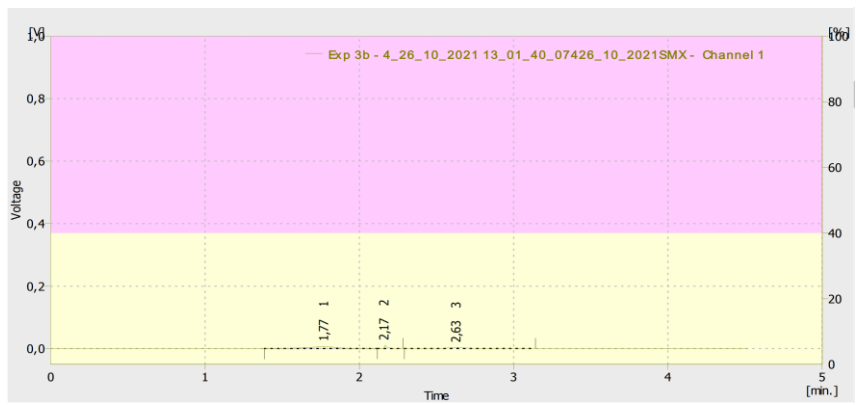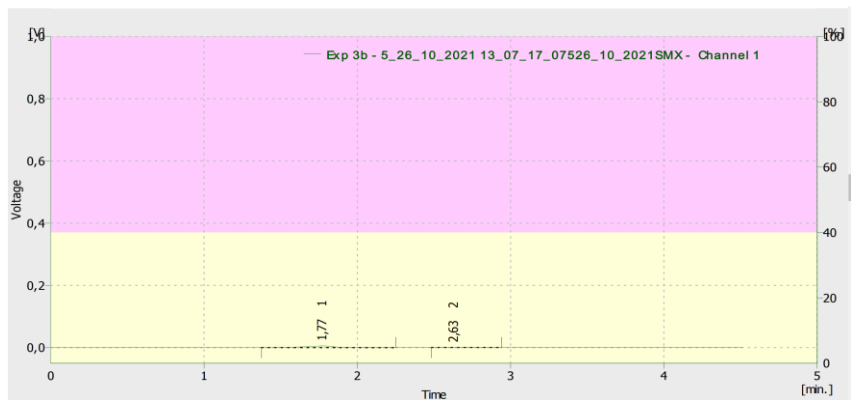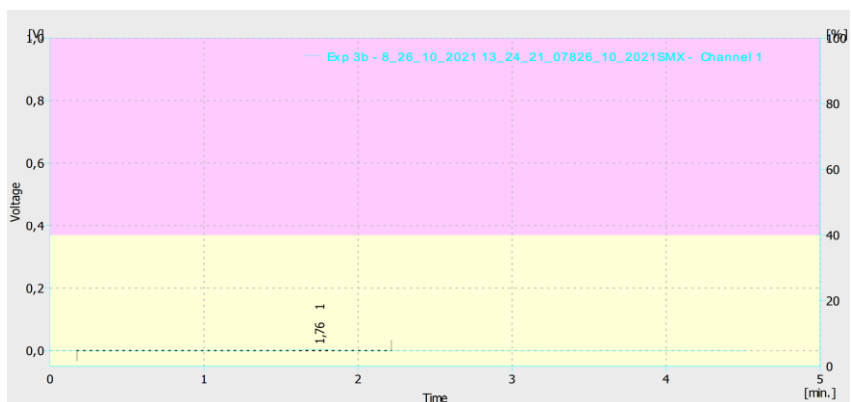
14. Annexes
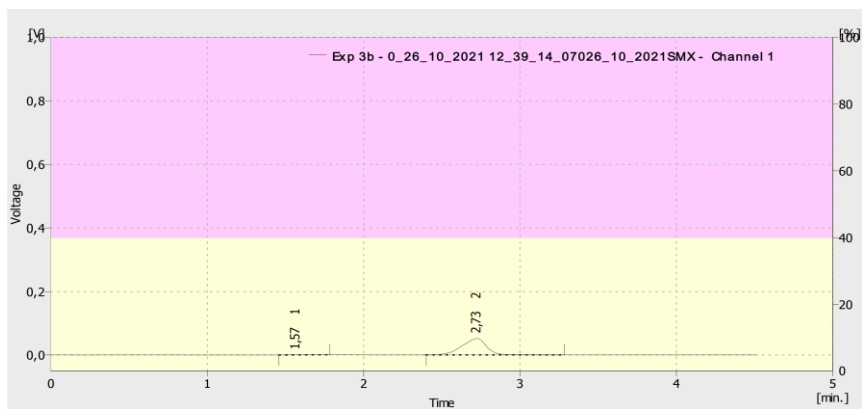
a)
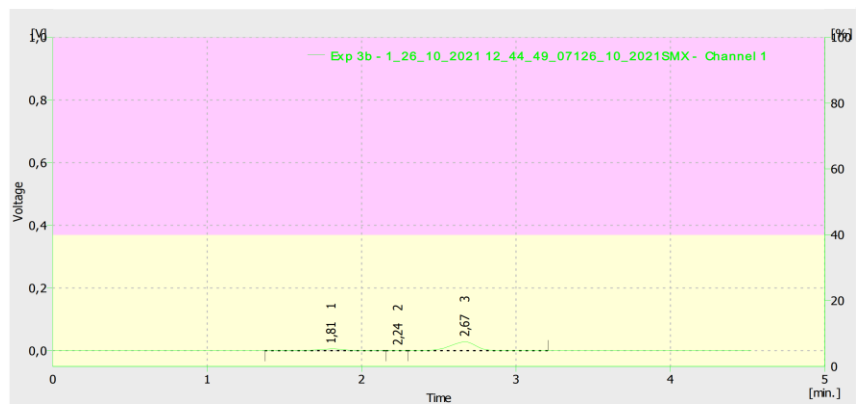

b)

c)

d)

e)

f)
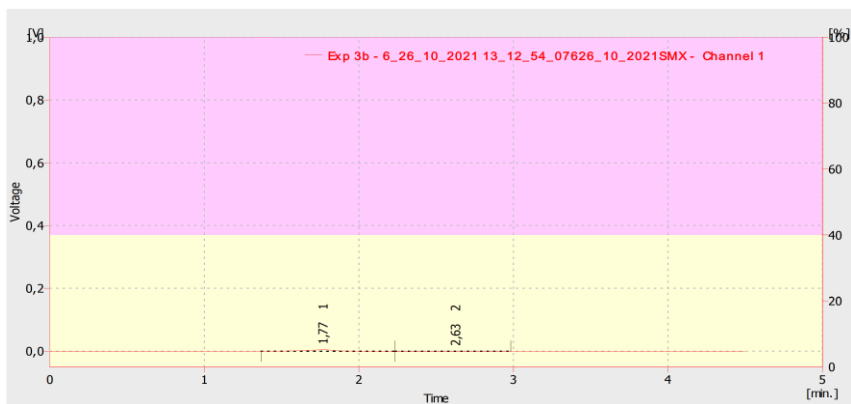
g)
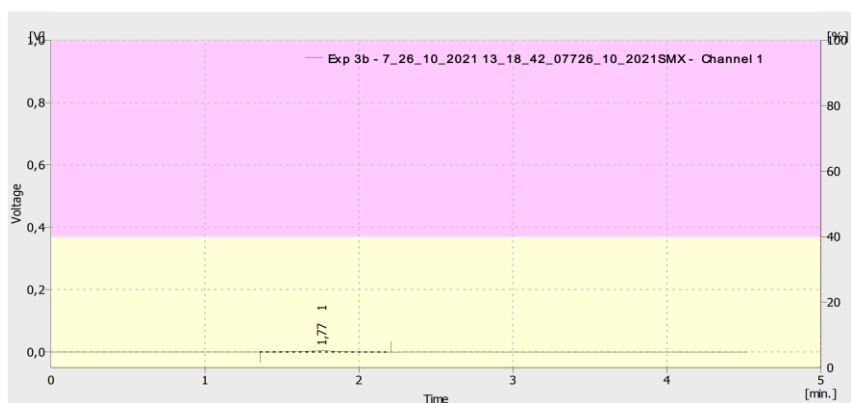
h)

i)

Fig. 1. (a-i) Chromatograms obtained during the SMX degradation with 0.3 g/L of TiO$_2$.

The chromatograph in Fig 1a) shows at 2.75 minutes the peak corresponding to SMX solution with the initial concentration of 10 mg/L. The chromatographs in Figures 1b) to 1i) show that the SMX peak decreases indicating the degradation of the SMX molecule. On the other hand, new peaks are formed proving the generation of intermediates that disappear with time justifying the decomposition of the molecule. This is in good agreement with the more than 70 % of mineralization obtained.
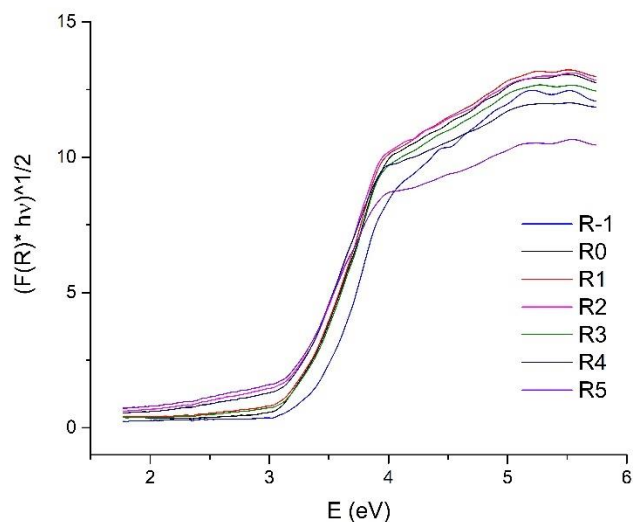
Fig. 2. Method of band gap energy (Eg) determination from the Tauc plot. The linear part of the plot is extrapolated to the x-axis. R_{-1} stands for the fresh catalyst, R_0 for the TiO_2 catalyst used for the first time, and $R_{i, i=1,5}$ for the ith cycle of the catalyst reuse.

a)

b)

Isotherm Linear Plot

● Fifth catalyst reuse   ▲ Fresh catalyst
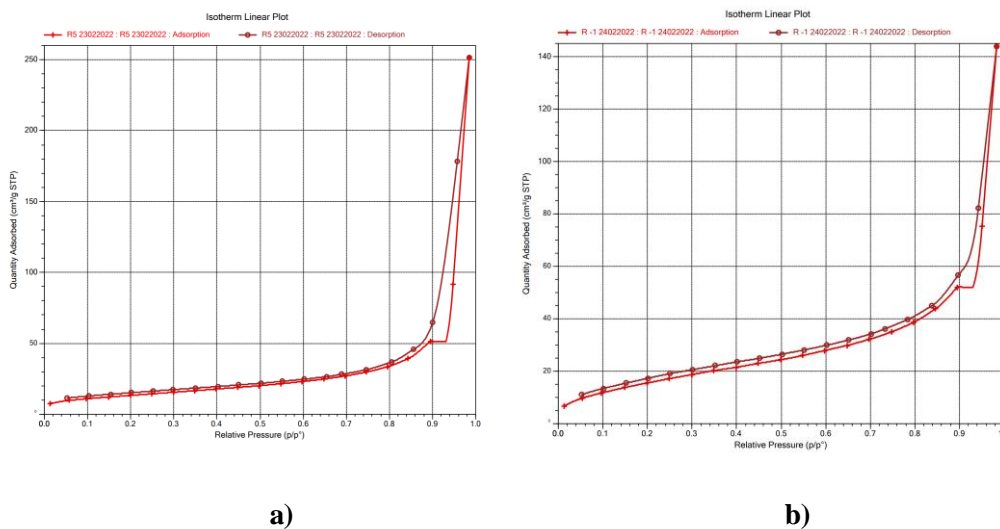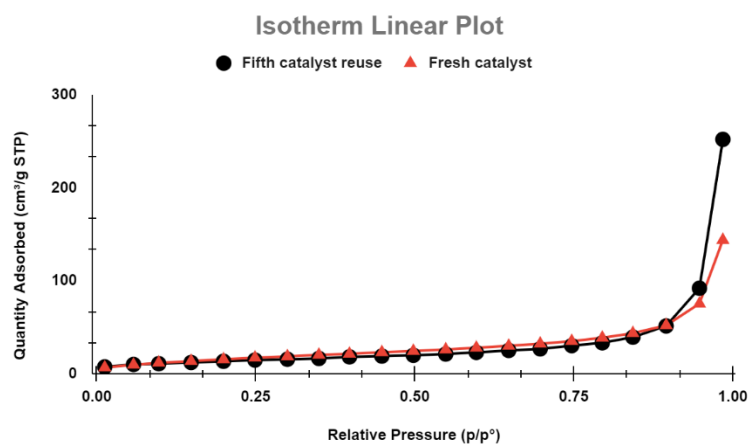
c)

Fig. 3. (a-c) The nitrogen adsorption-desorption isotherms using the Brunauer–Emmett–Teller (BET) method for TiO_2 catalyst. a) stands for the fifth cycle of the catalyst reuse, b) for the fresh catalyst, and c) combined both (only adsorption in c). In c), the red and the black lines stand for the fresh catalyst and the fifth cycle of the catalyst reuse).